

1 **Key parameters affecting induced seismicity in geothermal reservoirs across scale**

2 Hannes Hofmann¹, Yinlin Ji¹, Mauro Cacace¹, Arno Zang¹, Günter Zimmermann¹, Serge
3 Shapiro²

4 ¹*Helmholtz Centre Potsdam GFZ German Research Centre for Geosciences, Potsdam,*
5 *Germany*

6 ²*Freie Universität Berlin, Berlin, Germany*

7 **Summary**

8 In the frame of the energy transition the number of geothermal projects worldwide is rapidly
9 increasing. One important factor that hinders an even faster and more widespread utilization of
10 geothermal energy is the risk of induced seismicity associated to geothermal operations. It is
11 therefore required to improve the understanding of the key parameters affecting induced
12 seismicity due to cold water injection in geothermal systems. Of particular interest is the
13 influence of operational parameters such as injection temperature, injection pressure, injection
14 rate, injected volume and distance to faults and the influence of geological boundary conditions
15 such as rock properties, fault properties and the in-situ and dynamic stress field on induced
16 seismicity. The effect of temperature is of particular importance, as cascade utilization of
17 geothermal resources becomes more important to increase geothermal energy efficiency and
18 this results in lower re-injection temperatures.

19 Therefore, we provide an overview of the state-of-the-art knowledge on induced seismicity in
20 geothermal projects with focus on temperature effects. This literature study includes a summary
21 of relevant physical processes, modelling approaches, and a review of selected laboratory and
22 mine scale experiments as well as field scale examples of injection-induced seismicity in
23 geothermal reservoirs. We differentiate between mechanical, hydraulic and thermal processes,
24 highlight relevant coupled processes, and explicitly describe the influence of geological

25 parameters, operational parameters and the effect of temperature on injection-induced
26 seismicity. Based on this we discuss different seismic risk mitigation measures for geothermal
27 operations. This will allow to develop better guidelines and tools for exploration, development
28 and operation of geothermal systems.

29

30 **1. Introduction**

31 Induced seismicity refers to typically minor earthquakes (EQ) and tremors that are caused by
32 human activity that alters stresses and strains in the Earth's crust. There are a number of ways
33 in which induced seismicity has been seen to occur (Trifu 2002, 2010). Among these are large,
34 water-filled dam structures (reservoir-induced seismicity), underground rock excavations
35 (mining-induced seismicity), construction works, hydraulic fracturing, waste water injection,
36 carbon capture and storage and the extraction of oil, gas and geothermal energy (Foulger et al.,
37 2018).

38 Induced seismicity in geothermal settings has been documented for over thirty years in such
39 areas as Indonesia, the Philipinians, Japan, North and South America, New Zealand as well as
40 Europe (Foulger et al., 2018). In most cases thousands of earthquakes per year are generated
41 during development and exploitation of a geothermal field, but usually most of these
42 microquakes are below local magnitude $ML=3$, and not felt by people. Recent sites in the Rhine
43 Graben structure such as Basel (CH), Landau (D), Soultz-sous-Forêt (F) and Strasbourg (F)
44 have been experienced moderate seismicity (up to $ML=3.9$) due to EGS activities (Schmittbuhl
45 et al. (2021). Although this seismicity has been short lived it has attracted public interest due to
46 its location nearby densely populated areas. At other sites, the induced seismicity may be
47 entirely of low magnitudes, or due to the geologic boundary conditions (high attenuation of
48 seismic rays due to sediment cover, e.g. Groß-Schönebeck) below detection limit (Kwiątek et
49 al., 2010).

50 Seismicity induced or triggered by geothermal field operations, including re-injection in
51 hydrothermal systems (e.g., Californie and The Geysers) and stimulation of Enhanced
52 Geothermal Systems (e.g., Basel and Pohang), is a major risk hindering a more vivid market
53 uptake of this promising alternative energy source. In some cases, geothermal projects were
54 stopped due to induced seismicity (e.g., Basel, St. Gallen, Pohang) while others were stopped

55 (e.g., Mauerstetten) or significantly delayed (e.g., Haute-Sorne) before project start due to
56 reduced public acceptance resulting from induced seismicity in other geothermal projects. The
57 example of the Pohang EGS site with a related Mw 5.5 event shows that even large magnitude
58 events may be triggered by geothermal operations (Lee et al., 2019). Nevertheless, the vast
59 majority of geothermal projects does not induce any detectable seismic events, including
60 examples such as the Groß Schönebeck EGS, where even massive large volume (13000 m³)
61 cold water injection at very high flow rates (up to 9 m³/min) and wellhead pressures (up to ~59
62 MPa) did not result in any seismicity larger than Mw -1.0 (Kwiatek et al., 2010).

63 Due to its large technical/geological and societal importance, the topic of induced seismicity
64 was extensively studied at laboratory, mine, and field scale. Dedicated reviews of induced
65 seismicity in geothermal reservoirs summarize our current understanding of the underlying
66 processes (Buijze et al., 2020; Evans et al., 2012; Gaucher et al., 2015; Zang et al., 2014; Ji et
67 al., 2022).

68 While significant progress on the understanding of induced seismicity in geothermal reservoirs
69 was made, the role of key operational and geological parameters still needs to be better
70 understood. Therefore, we summarize how these parameters affect induced seismicity in
71 geothermal reservoirs at laboratory, mine, and field scale and discuss the different observations
72 at different scales for the key parameters (Figure 1). A focus of this review is on thermal effects
73 as large temperature differences between injection fluid and reservoir are particularly important
74 for geothermal operations compared to all other subsurface operations stated above. These
75 temperature effects are long-term effects as the cold water plume slowly, but steadily develops
76 over the decades of cold water injection in geothermal reservoirs. We highlight common
77 observations at all scales, discrepancies and knowledge gaps in order to facilitate future
78 experiments and model development. Based on this review, we will also propose implications
79 for geothermal operations with reduced seismic risk.

80 2. Theory and models

81 2.1. Statistics based seismicity models

82 Statistical models for induced seismicity aim at characterizing the observed seismic event
83 population based on a statistical model. Usually these approaches rely on a Gutenberg-Richter
84 (GR) frequency-magnitude statistics to extrapolate from relatively small sized events to large
85 earthquakes and to estimate the expected event population at the end of an operational activity.
86 Based on the GR law, the cumulative number of earthquakes with magnitude greater than M is
87 given by:

$$88 \log N_{>M} = a - b M \quad (1)$$

89 where a and b are considered as constants, with the former parameter providing a measure of
90 the seismic intensity and the b -value generally consider to be near 1. To apply this statistical
91 framework to reservoir induced seismicity the assumptions are made that the event magnitudes
92 obey the GR statistics, that the seismicity rate is related to the fluid injection rate, and the
93 cumulative seismicity is related to the total injected volume (Shapiro 2010). This is a result of
94 (i) the assumption that the seismicity is triggered by pore pressure perturbations and (ii) of the
95 application of the fluid mass conservation law. The GR relationship, derived based on the
96 recorded seismicity at the early stages of the reservoir operations, is then extrapolated to the
97 final time of the operation to provide the final estimate for the event population. The obtained
98 population statistics can be further used to forecast the largest sized event expected also in
99 relation to relatively few operational parameters.

100 To derive the cumulative number of induced earthquakes, there are some assumptions that must
101 be fulfilled. Injection is usually approximated by a point-like source inside a porous domain
102 consisting of a set of random oriented, non-interacting point-like defects (referred to as
103 fractures), the volume concentration of which (ζ) obeys a statistically homogeneous
104 distribution. Each fracture is characterized by its own critical failure state, being exemplified

105 by a critical pore pressure that must be overcome for a slip event to occur under a Mohr-
 106 Coulomb failure criterion (the parameter C in Shapiro et al., 2010). The critical pore pressure
 107 is randomly selected from a uniform distribution provided by an upper (C_{\max}) and lower (C_{\min})
 108 bound. There is no possibility to consider time-dependent fault healing after an earthquake has
 109 occurred.

110 The approximations described above yield the following formalism for the probability of an
 111 earthquake to occur at a given location:

$$112 \quad W_{ev}(r, t) = \int_{C_{\min}}^{p(r,t)} f(C) \sim \frac{p(r,t)}{C_{\max}} \quad (2)$$

113 The total number of induced earthquakes then can be derived as:

$$114 \quad N(t) = \frac{A\zeta}{C_{\max}} \int_R^{\infty} p(r, t) r^{\delta-1} dr \quad (3)$$

115 Where the factor A is a geometrical constant related to the dimension of the problem considered.
 116 δ is the spatial dimension of the diffusional process of the pore pressure relaxation and R
 117 describes the radius of an effective injection source. Dinske and Shapiro (2013) recast Equation
 118 3 in terms of the total injected fluid volume, $v(t) \sim \int_0^t Q_i(t) dt$ with $Q_i(t)$ being the injection
 119 rate, for generic injection scenarios as:

$$120 \quad N(t) = \frac{v(t)\zeta}{C_{\max} S} \quad (4)$$

121 where ρ_0 is the density of the fluid, considered constant, and S is the uniaxial storage coefficient.
 122 The GR statistics then leads to the following formulation for the cumulative number of events
 123 with magnitude higher than a given magnitude M and the log₁₀ probability of $M \geq 0$ a_w (a_w
 124 here is not the GR a -value):

$$125 \quad \log N_{>M}(t) = \log\left(\frac{v(t)\zeta}{C_{\max} S}\right) + a_w - bM \quad (5)$$

126 Or written in terms of the seismogenic index $\Sigma = a_w - \log(F_t S)$, with $F_t = \frac{C_{max}}{\zeta}$ being the
127 tectonic potential, as:

$$128 \log N_{>M}(t) = \log(v(t)) - bM + \Sigma \quad (6)$$

129 For example, a statistical analysis of the Basel EGS seismicity was performed by Bachmann et
130 al. (2011) to develop a probability-based seismic monitoring approach for EGS.

131 **2.2. Physics based reservoir modelling approaches**

132 The goal of physics based reservoir models of induced seismicity is to arrive at a quantification
133 of the seismic risk induced by subsurface operations by considering all relevant physical
134 processes. To achieve this goal the focus should be on a proper characterization of the thermal,
135 hydraulic and mechanical reservoir parameters and processes (Figure 2) including rock mass
136 deformation, pore pressure propagation, poro- and thermo-elastic stress transfer and failure
137 processes and by considering the presence of natural and induced hydrogeological and
138 mechanical heterogeneities, faults and fractures, their formations and interactions. The
139 challenge here is therefore to develop flexible numerical approaches that enable to consider the
140 relevant processes, and, most importantly, the non-linear feedback among them.

141 Induced or triggered seismicity is the result of slip of pre-existing fractures or faults. This slip
142 may be induced by a reduction of the effective normal stress on the fault through a pore pressure
143 increase, by poroelastic or thermoelastic stress changes, by stress changes caused by aseismic
144 slip and by changes of frictional properties of the fault as visualized in the Mohr-Coulomb plot
145 in Figure 3.

146 **2.2.1. Relevant source mechanisms of induced seismicity**

147 **Poro- and thermos-elasticity**

148 The physical framework relies on well-established conservation equations for the fluid and solid
 149 mass, internal energy and momentum which has to be closed by proper equations of state
 150 describing interactions among the difference processes and their influence on the evolution of
 151 the material properties of interest. To derive the basic equations we imply the following primary
 152 variables: temperature (T), pore pressure (p) and the solid displacement vector (**u**).

153 The mass balance equation of a porous media can be considered as a volumetric average of its
 154 fluid and solid (i.e. grains) components as (Cacace and Jacquey, 2017):

$$155 \frac{\varphi}{\rho_f} D_t^f \rho_f + \frac{(1-\varphi)}{\rho_s} D_t^s \rho_s + \nabla \cdot \mathbf{v}_s + \nabla \cdot \mathbf{q}_d = 0 \quad (7)$$

156 In equation 7, φ is the porosity, ρ_f and ρ_s are the fluid and solid density respectively, \mathbf{v}_s is the
 157 solid deformation velocity, $\mathbf{q}_d = \varphi(\mathbf{v}_f - \mathbf{v}_s) = -\frac{k}{\mu_f}(\nabla p - \rho_f \mathbf{g})$ is the Darcy velocity, μ_f
 158 is the dynamic fluid viscosity and D_t^f and D_t^s are the total (Lagrangian) derivatives with respect
 159 to a moving fluid and solid respectively.

160 Equation 7 can be recast in terms of the primary variables by the following considerations. The
 161 first term can be expressed as:

$$162 D_t^f \rho_f = \varphi \left(\frac{1}{K_f} D_t^f p - \beta_f D_t^f T \right) \quad (8)$$

163 where $\frac{1}{K_f} = \frac{1}{\rho_f} \left(\frac{\partial \rho_f}{\partial p_f} \right)_T$ is the reciprocal of the fluid compressibility (fluid bulk modulus) and

164 $\beta_f = -\frac{1}{\rho_f} \left(\frac{\partial \rho_f}{\partial T} \right)_{p_f}$ is the volumetric thermal expansion coefficient of the fluid. To recast the

165 second term in Equation 7 in terms of the primary variable requires the definition of a proper
 166 constitutive mechanical model. The latter can be derived from the linear momentum
 167 conservation ($\nabla \cdot (\boldsymbol{\sigma} - \alpha p \mathbf{I}) + \rho_b \mathbf{g} = 0$) under the assumption of linear Biot's poroelastic
 168 framework as:

169 $\dot{\sigma}_{ij} = C_{ijkl}\dot{\epsilon}_{kl}^e$ (9)

170 where C_{ijkl} is the elastic stiffness tensor and α is Biot's coefficient.

171 By taking into consideration Equations 8 and 9, and by neglecting second order non-linear
172 advective terms, it is possible to rewrite equation 7 as:

173 $\frac{1}{M_b} \frac{\partial p}{\partial t} - \alpha_b \frac{\partial T}{\partial t} - (1 - \alpha)\dot{\epsilon}_{kl}^e + \dot{\epsilon}_{kk} + \nabla \cdot \mathbf{q}_D = 0$ (10)

174 In equation 10 M_b is the Biot Modulus, α_b is the bulk thermal expansion coefficient and we
175 make use of the following relation $\nabla \cdot \mathbf{v}_s = \nabla \cdot \dot{\mathbf{u}} = \dot{\epsilon}_{kk}$.

176 Equation 10 does not consider any irreversible (other than elastic) deformation mechanism. The
177 latter can be integrated by relying on the eigenstrain formulation. When assuming a small strain
178 formulation the total strain (ϵ) can be split into the sum of an elastic reversible strain component
179 (ϵ^e) and an inelastic irreversible strain component (ϵ^*). Therefore Equation 10 takes the
180 following form:

181 $\frac{1}{M_b} \frac{\partial p}{\partial t} - \alpha_b \frac{\partial T}{\partial t} - \alpha \dot{\epsilon}_{kk} + (1 - \alpha)\dot{\epsilon}_{kk}^* + \nabla \cdot \mathbf{q}_D = 0$ (11)

182 In a similar way as above, it is possible to derive an evolution equation for the porosity as:

183 $\frac{\partial \phi}{\partial t} = \frac{(\alpha - \phi)}{K_s} \frac{\partial p}{\partial t} - \alpha_b \frac{\partial T}{\partial t} - (\alpha - \phi)\dot{\epsilon}_{kk} + (1 - \alpha)\dot{\epsilon}_{kk}^*$ (12)

184 The internal energy balance of the porous medium, under thermal equilibrium between the solid
185 and fluid phase, and by considering additional thermoelastic dissipative mechanisms reads as:

186 $T \frac{\partial(\rho c)_b}{\partial t} + (\rho c)_b \frac{\partial T}{\partial t} + T_0 \beta_b \dot{\epsilon}_{kk}^e + \nabla \cdot (\rho_f c_f \mathbf{q}_D T - \lambda_b \nabla T) - \dot{H} = 0$ (13)

187 with

188 $T \frac{\partial(\rho c)_b}{\partial t} = (1 - n)c_s T \left(\frac{\rho_s}{K_s} \frac{\partial p_f}{\partial t} - \rho_s \beta_s \frac{\partial T}{\partial t} \right) + n c_f T \left(\frac{\rho_f}{K_f} \frac{\partial p_f}{\partial t} - \rho_f \beta_f \frac{\partial T}{\partial t} \right)$ (14)

189 Equation 13 can be modified to take into account additional thermal effects resulting from fluid
190 dilation or shear heating. Large pore pressure build-up or thermal stress can bring the reservoir
191 partially to the inelastic regime by mechanisms of hydraulic fracturing (Li et al., 2020) and
192 thermal shock (Zhou et al., 2017).

193 **Non-linear pore pressure diffusion**

194 Injection-induced seismicity is highly dependent on fluid pressure build-up and migration in
195 the faulted reservoir (Cappa et al., 2018), so it is crucial to accurately model the pore fluid
196 diffusion. As pointed out by Zhang and Mehrabian (2020), in most previous models, the pore
197 pressure diffusion is modelled using a constant permeability tensor. However, the evolution in
198 space and time of a pore pressure front within a porous fractured medium has a non-linear
199 dependency on the permeability (a tensorial quantity) and, for fracture flow, on the hydraulic
200 aperture of the fracture. These quantities are rarely constant in space and time, but vary as a
201 function of the in-situ stress, and for fault zones also in terms of the shear- and normal-slip.
202 There is a series of publications considering non-linear pressure diffusion as a triggering
203 mechanism of induced seismicity. They consider the hydraulic diffusivity as a function of the
204 pore pressure (exponential or power law functions) and include a detailed analysis of the
205 diffusion fronts (e.g., Shapiro and Dinske, 2009; Hummel and Shapiro, 2013; Johann et al.,
206 2016).

207 The hydraulic behaviour of fractured reservoirs is highly dependent on the fluid properties of
208 embedded clusters of joints, fractures and fault zones. The hydro-mechanical behaviour of these
209 geological discontinuities is sensitive to variations of the effective normal stress and shear
210 displacement. Variations in the hydraulic aperture a_H of a failure plane based on a varying
211 effective normal stress is usually formulated as an exponential (hyperbolic) functional
212 relationship as:

$$a_H = a_{sat} + a_0 e^{\left(\frac{\sigma'}{\sigma^*}\right)}, \quad (15)$$

where a_{sat} is the aperture residual at saturation (lower bound), a_0 is a reference aperture (upper bound) and σ^* is an experimentally constrained stress sensitivity parameter. Of particular relevance for reservoir induced seismicity studies is to understand the role of induced shear-slip and stress (hydro-shearing) on the evolution of the fault hydraulic properties. Rinaldi & Rutqvist (2019) presented a fracture aperture model that combined the above described evolution with additional effects from shear-induced aperture increase (a_{shear}) and tensile opening ($a_{tensile}$). In their model, these correction terms in the fracture aperture are computed as a function of the resolved plastic strain (ε_p) upon fault reactivation, once again described in term of a Mohr-Coulomb failure criterion as:

$$\begin{cases} a_{shear} = \varepsilon_{ps} \tan(\varphi) / s_f \\ a_{tensile} = \varepsilon_{pt} w \end{cases} \quad (16)$$

In Equation 16 φ is the dilation angle, ε_{ps} and ε_{pt} are the plastic strain under shear and tensile failure respectively, s_f is the fracture spacing, which is determined by the number of fracture per unit of width (w) of fracture area.

Fault strength is controlled by variations in the effective stress as well as in the fault friction coefficient. In the earthquake modelling community attention has been towards quantify the effects of the latter parameter (see also next paragraph) in the context of empirical rate and state formulations including weakening mechanisms relevant at co-seismic slip rates. Relative few works have been focused on a better description of the role of pore pressure variations both during the inter-seismic and co-seismic stage and their effects on the fault stability (Section 3). As already stated above, the hydraulic properties of fault zones should be considered as dynamic quantities during the life time of an operational reservoir. Drained triaxial experiments on porous samples having a predefined fault have revealed the importance of variations in the fault permeability in inducing pore pressure transients (fault valving behaviour) and dynamic

237 weakening followed by dilatant-enhanced strengthening of the same sample. Such transients
 238 have been interpreted in terms of non-linear feedback loops between the shear-slip enhanced
 239 permeability, healing processes (pressure solution) and permeability variations due to change
 240 in the mechanical loading of the pores. To a first order, these non-linear interactions can be
 241 captured by a non-linear model for the fault permeability that takes into account both its
 242 sensitivity to normal stress variations (Equation 15) and the additional shear-slip permeability
 243 enhancement and healing processes as (Zhu et al., 2020):

$$244 \quad k = k_{sat} + (k^* - k_{sat})e^{\left(\frac{\sigma'}{\sigma^*}\right)} \quad (17)$$

245 Equation 17 describes a permeability evolution similar to the one described above in Equation
 246 15, but enables to capture additional mechanical and chemical feedback by setting a proper
 247 evolution law for the reference permeability variable (k^*). Zhu et al. (2020) derived a simple
 248 formulation to describe both permeability enhancement by shear-slip and fault healing:

$$249 \quad \frac{\partial k^*}{\partial t} = -\frac{v}{L}(k^* - k_{max}) - \frac{1}{T}(k^* - k_{sat}) \quad (18)$$

250 The first term on the right hand side of Equation 18 describes the effects of shear-slip
 251 permeability increase up to a maximum permeability value (k_{max}) as a function of the resolved
 252 slip velocity (v) over a given slip distance (L). This latter parameter can be physically
 253 interpreted as an hydraulic estimate of the critical friction distance (d_c) for breakdown of
 254 frictional strength in rock, which can be constrained by laboratory evidence. The second term
 255 in Equation 18 describes fault healing and permeability reduction down to its saturation value
 256 (k_{sat}) over a characteristic healing time scale (T). This latter parameters lacks a unique
 257 experimental description, mainly because of the different time scales involved in the healing
 258 and sealing processes. Worth mentioning is that the healing term can be extended to include
 259 thermal effects (pressure solution) by setting the healing time dependent on the background
 260 temperature conditions.

261 **Shear slip induced stress transfer**

262 Shear stress transfer induced by aseismic fault slip has been recognised as an important driven
263 source of seismic events (Cappa et al., 2018; Ji et al., 2021a). Shear slip on fault planes induces
264 not only variations in the hydraulic properties of the faults, but it also acts as a source of a
265 (quasi)static stress transfer, which likely affects faults' stability. Only recently this stress
266 component has received some attention and there is an increasing number of works that have
267 identified it as relevant to explain field observations as post shut-in seismicity (Deichmann et
268 al., 2014 for the Basel EGS). Mesoscale fluid injection experiments (Section 4) have also shed
269 light on the role of stress transfer during aseismic slip in triggering earthquakes far beyond the
270 pressurized fault domain (Cappa et al., 2018). In order to include this additional components in
271 the fault stress balance equation, we here consider a poroelastic medium under a small strain
272 approximation. Therefore we can make use of the principle of superposition to compute the
273 total stress acting on the fault as:

$$274 \sigma_{tot} = \sigma_{res} + \delta\sigma \quad (19)$$

275 Equation 19 takes into account both the loading induced from the interaction with the reservoir
276 (first term) as well as those included by fault slip (normal and shear). The last term in Equation
277 19 can be further split into a quasi-static component (elastic stress transfer due to slip) and into
278 a dynamic component associated with propagation of elastic waves ($\delta\sigma = \delta\sigma_{QS} + \delta\sigma_D$). Note
279 that the shear and normal traction acting on the fault are directly obtained from Equation 19.
280 The inertial terms in Equation 19 due to elastic wave propagation can be either treated explicitly
281 (full inertial system) or can be approximated (damped system following Rice, 1993) as:

$$282 \delta\sigma_D \sim \beta_{rad}V, \quad (20)$$

283 where v is the slip velocity (time derivative of the resolved slip on the fault plane) and $\beta_{\text{rad}} (=$
 284 $\frac{G}{2c_s}$ with G being the shear modulus and c_s the shear wave velocity) is the radiation damping
 285 coefficient. Therefore, the final stress balance reads as:

$$286 \quad \tau_{\text{res}} + \delta\tau_{\text{qs}} - \beta_{\text{rad}}v = \mu (\sigma'_{\text{res}} + \delta\sigma_{\text{qs}}) \quad (21)$$

287 With the friction coefficient μ . Shear stress transfer, as an indirect effect of fluid injection,
 288 should be taken into consideration because it can trigger seismicity in unpressurized/untargeted
 289 formations (e.g., Guglielmi et al., 2015a; Kolawole et al., 2019).

290 **2.2.2. Slip tendency analysis**

291 The reactivation potential of fault zones during reservoir operation is usually quantified by a
 292 Slip Tendency (ST) analysis. The goal of a ST analysis is to identify which planes of weakness
 293 are close to be reactivated under a certain stress state as locally perturbed by operational
 294 activities. A ST analysis describes fault stability in terms of a stress balance, where the stress
 295 acting on a specific fault is resolved into a normal - stabilizing - and shear - destabilizing -
 296 component. Cauchy's theorem can be used to compute the normal and shear component of a
 297 stress tensor (described in term of its normal traction \mathbf{t}_n) acting on a fault plane described by a
 298 unit normal (\mathbf{n}) as:

$$299 \quad \begin{cases} \|\sigma\| = \mathbf{t}_n \cdot \mathbf{n} \\ \|\tau\| = \sqrt{\|\mathbf{t}\|^2 - \|\sigma\|^2} \end{cases} \quad (22)$$

300 Following this theoretical framework, fault stability, or better, the potential for fault
 301 reactivation, can be simply described by the a scalar quantity, the ST, given by the ratio of the
 302 destabilizing and the stabilizing force under a certain metric, for which the L2-norm is usually
 303 considered:

$$304 \quad \text{ST} = \frac{\|\tau\|}{\|\sigma - \alpha p\|}, \quad (23)$$

305 where the term at the nominator is the shear stress acting on the fault plane, and the quantity at
 306 the denominator defines the effective normal stress assuming Biot's theory of poroelasticity.
 307 From Equation 23 it is clear that higher values of ST will indicate a higher reactivation potential
 308 for a given fault. In order to be of any practical use in the context of induced seismicity studies,
 309 Equation 23 should be cast in terms of a failure criterion in order to provide upper and lower
 310 bounds for the ST parameter range. In reservoir analysis, it is often common to rely on the
 311 Mohr-Coulomb failure theory, which relates the shear strength of a fault τ_s to the in situ stress
 312 via two material properties, that is, the static friction coefficient (μ_0) and the cohesive fault
 313 strength (C) as:

$$314 \quad \tau_s = \mu_0 (\sigma - \alpha p) + C \quad (24)$$

315 For some rock types, the intermediate principal stress plays a role, and Mohr-Coulomb is not
 316 valid (Labuz and Zang, 2012). Blöcher et al. (2018) used a true-triaxial failure criterion to
 317 account for this. In both cases, it follows that slip on a fault will only occur if the fault stress
 318 balance (Equation 24) is not satisfied, that is, if the current stress state acting on a fault exceeds
 319 the fault shear strength:

$$320 \quad \|\tau\| \geq \|\tau_s\| \quad (25)$$

321 By rearranging the above equations, one arrives at a functional description of the ST parameter
 322 that can be used to quantify the reactivation potential of a certain fault under a given stress state
 323 with proper physical bounds as dictated by the fault mechanical properties and its geometry:

$$324 \quad ST \geq \frac{C}{\|\sigma - \alpha p\|} + \mu_0 \quad (26)$$

325 Commonly faults are considered as having no residual cohesive strength, therefore the stability
 326 condition described in Equation 26 can be further simplified as:

$$327 \quad ST \geq \mu_0 \quad (27)$$

328 Equation 27 relates the fault reactivation potential to one single fault parameter, that is the static
329 friction coefficient. Experimental works done by Byerlee in the late 1970s provided estimates
330 for this parameter, the latter being independent of the specific rock type and only slightly
331 dependent on the mean stress. Following the work by Byerlee (1978), μ_0 should be considered
332 to be greater than or equal to 0.85 for confining pressure up to 200 MPa and greater than or
333 equal to 0.6 at higher confining pressure. More recent works by Zoback (2007) have also
334 identified a functional dependence of the static friction coefficient with respect to the mineral
335 assemblage of the porous rock sample, where the presence of phyllosilicates results in lower
336 values of μ_0 . Despite these experimental evidence, for a ST analysis the value of the friction
337 coefficient is usually considered as constant, following Byerlee's law. Once the slip tendency
338 on a particular fault is computed, it is then possible to quantify the overpressure threshold for
339 fault instability to occur, that is the amount of over-pressure induced to promote slip.

340 A slip tendency analysis was performed to assess induced seismicity for example at the Groß
341 Schönebeck EGS site in the North German Basin (Blöcher et al., 2018) and Hydrothermal
342 systems in the Bavarian Molasse Basin (Budach et al., 2017; Ziegler and Heidbach, 2020).

343 **2.2.3. Coulomb failure stress change model**

344 Another model to compute fault instability and related seismic hazard during fluid injection and
345 production in geothermal reservoirs relies on the concept of Coulomb failure stress (CFS)
346 variations. The theoretical framework that underlies the Coulomb Stress Change model
347 (Δ CFS model hereafter) is similar to the one described above for the ST model. A Δ CFS model
348 also relies on the concept of Mohr-Coloumb-like failure to map the onset of instabilities and
349 the consequent seismic slip of a fault of a given orientation. The basic idea is that fault stability
350 is controlled by resolved variations with respect to an undisturbed (tectonic stressing) state,
351 with positive changes favouring the generation of seismic events and negative values
352 contributing to fault stabilization. These variations can be postulated into the following form

353 (compressive stress are assumed here as negative, which is the material sciences stress
354 convention, not the geosciences stress convention):

$$355 \quad \Delta\text{CFS} = \Delta\tau - \mu(\Delta\sigma - \alpha\Delta p) \quad (28)$$

356 The historical development of the ΔCFS model dates back to studies in the 1980s (Stein and
357 Lisowski, 1983) and 90s (e.g., Harris and Simpson, 1992) that aimed at modelling aftershock
358 sequences after large or intermediate size events and/or earthquake swarms in volcanic settings.
359 Only recently, this model has been used in the context of injection induced seismicity (e.g.,
360 Catalli et al., 2013). The most appealing aspect of such model stems from its simple theoretical
361 framework that makes it easy to be integrated in any reservoir simulation software. In the
362 context of reservoir simulation, the main improvement compared to the classical ST concept is
363 that this model can consider, within assumptions as detailed below, the role of (poro)elastic
364 stress transfer, that is to consider the dynamics responsible for communicating a developed
365 stress perturbation (origin) to a particular fault (receiver). The ability to capture in a rather
366 simple numerical formulation both long-range (quasi)static and dynamic (pore pressure effects)
367 interactions over time makes such model useful in the context of seismic hazard studies of
368 geothermal reservoirs.

369 The ΔCFS model assumes the existence of a stress change threshold for triggering instability.
370 To quantify the validity of this assumption a number of studies focused on establishing
371 correlations between the existence and magnitudes of this „triggering stress threshold“ to the
372 particular geological site and, in particular to the type of faulting. With respect to the latter
373 aspect, despite all efforts, there seems to be a lack of a clear correlation between the faulting
374 regime, measured variations in failure rates and the stress change estimates derived from this
375 model.

376 A CFS model was applied by Parisio et al. (2019) to assess the risk of long-term re-injection in
377 supercritical geothermal systems. They highlight the importance of thermal stresses on fault

378 reactivation potential in supercritical systems. The approach is also used for induced seismicity
379 related to other fluid injection operations such as the Central Oklahoma waste water injection
380 site (Johann et al., 2018).

381 One of the main effects of operational activities on fault planes is to promote dynamic frictional
382 weakening thereby inducing shear-slip (and possibly dilation) along the fault. In the context of
383 the Δ CFS model, variations in resolved Coulomb stress can provide useful to estimate the
384 amount of induced slip on the fault thereby providing an estimate of the driving force for shear
385 displacement (excess shear stress or $\Delta\tau_s$). By relying on classical concepts from linear elastic
386 fracture mechanics (LEFM), the excess shear stress can then be used to compute the magnitude
387 of shear displacement (u_s) once the shear stiffness (K_s) of the fault plane is given as:

$$388 \quad u_s = \frac{\Delta\tau_s}{K_s} \quad (29)$$

389 Having computed the shear-displacement from Equation 20, it is then possible to obtain the
390 seismic moment by:

$$391 \quad M_0 = \int G u_s dA, \quad (30)$$

392 where G is the shear modulus and the integration is done over the area of the fault over which
393 slip occur.

394 By a closer inspection to Equation 28 it is possible to identify the presence of three distinctive
395 (though mutually interacting) stress components in the model that is, (i) variations in shear and
396 (ii) (effective) normal stress and (iii) friction coefficient. If one assumes a constant tectonic
397 stressing rate and friction coefficient, the main stress parameter affecting the evolution of the
398 Coulomb stress is provided by pore pressure variations only. For reservoir operations those
399 variations are driven by operational activities and (at timescales that are relevant for reservoir
400 activities) the drained response of the porous medium to those variations. Therefore, for this

401 specific case, the predictions from the Δ CFS model closely match those obtained from
402 seismicity rate approaches as based on the concept of a (non)linear diffusion front.

403 This observation has led to the development of what can be referred to as hybrid approaches
404 that combine concepts from physics-based forward reservoir modelling to those based on
405 statistical analysis. Shapiro et al., (2010) introduced the concept of the seismogenic index to
406 quantify the probability of an induced event within a specified time window. In their original
407 formulation, Shapiro et al (2010) assumes nonlinear pore pressure relaxation as the triggering
408 mechanism for induced events within a porous medium consisting of a statistically random
409 distribution of pre-existing cracks approximated as point source defects. The main assumption
410 is to assume the seismogenic index to be proportional to the maximum pore pressure
411 perturbation only. This assumption can be extended to take into consideration the resolved
412 variation in Coulomb stress changes as described above, thereby proving a link between the
413 statistical approach and dynamic reservoir modelling. Shapiro (2018) provided the theoretical
414 framework to generalize the original approach centred on a pore pressure perturbation
415 formalism for induced seismicity to a more general formalism taking into account the full
416 poroelastic coupling. In his approach, he considered that the failure criterion described in terms
417 of Coulomb stress changes can approximate the criterion for earthquake occurrence and,
418 consequently, the former parameter can be used to estimate the number of earthquakes at a
419 given location. By assuming a statistical distribution for the Δ CFS on given faults, it follows
420 that the total number of induced earthquakes can be computed by multiplication of the
421 volumetric integral of the probability for each fault to fail seismically time the density
422 concentration of faults in the reservoir. The former probability distribution is then given by the
423 integral over the whole reservoir domain of the resolved Δ CFS during the elapsed time, or, in
424 simpler words, the total number of expected earthquake in a given volume of a reservoir and at
425 a given time is proportional to the volume integral of the variations in Coulomb Stress changes.

426 It follows that the seismicity rate can be computed by taking the time derivative of the
427 probability density function as:

$$428 \quad S(t) = \int_V \frac{\partial \Delta CFS}{\partial t} H(\Delta CFS - C_{\min}) H(C_{\max} - \Delta CFS) dv \quad (31)$$

429 In Equation 22 $H(\Delta CFS - C_{\min})$ and $H(C_{\max} - \Delta CFS)$ are Heaviside functions that
430 represents lower and upper bounds of the probability density function, respectively.

431 **2.2.4. Rate and state friction**

432 The strength of Earth's crust is classically approximated by a rheological model that portrays
433 a, more or less gradual variation with increasing depth (and therefore mean stress) from brittle
434 frictional deformation at shallower depths given way to a more (frictional) ductile non-dilatant
435 deformation at greater depth. The Brittle Ductile Transition (BDT) is defined as a domain of
436 finite extent where this transition occurs at depth. The BDT depth extent is constrained in a
437 range of around 10/20 km, thereby encompassing the depth interval where the majority of
438 earthquakes occur, that is, the BDT provides a conservative estimate of the depth extent of the
439 seismogenic zone. Within the seismogenic zone, faults display 'frictional-elastic-viscous'
440 deformation at steady tectonic slip rates described by cataclastic processes with a linear
441 dependency on the effective normal stress and, under specific background conditions also
442 viscous-like deformation processes, typically pressure solution creep. View in this context,
443 earthquakes (also induced ones) are thought as the consequence of a sudden release of energy
444 during rapid slip (slip velocity of the order of m/s) on active (reactivated) geological faults.
445 These observations support a phenomenological description of earthquakes as analogous to
446 frictional (stick-slip) instability as usually observed in laboratory rock friction experiments.
447 This phenomenological description also agrees with observations that show a multi-scale self-
448 affine structure of faults along a wide range of dimensions, with shear strain localization
449 occurring principally into a narrow principal slip zone (PSZ). This is suggestive that the

450 rheology of the fault rock or “gouge” within the PSZ might control to a first order the
451 macroscopic fault behaviour. Experimental evidence for such behaviour firstly came from the
452 works of Byerlee (1970) who demonstrated how frictional instability could arise from the
453 sudden weakening of the fault interface combined with a low shear stiffness of the surrounding
454 medium. Within a frictional framework, weakening arises from variations in the friction
455 coefficient from its initial value, following therefore a dynamic friction model. Two basic
456 observations that are important in this context are the fact that (i) dynamic slip can be achieved
457 only after a finite amount of slip, and that (ii) the frictional state is a function of the slip velocity
458 and maintains a sort of „state memory effect“. Later experimental evidence on the existence of
459 repetitive (stick-slip) instabilities in the laboratory highlighted the importance of fault healing
460 in addition to the slip induced weakening.

461 Those experimental evidence were finally combined into an empirical formulation known as
462 Rate and State Friction (RSF hereafter). In its classical formulation derived by Deiterich (1970)
463 and Ruina (1983), the friction coefficient appearing in the fault stress balance equation
464 (Equation 31) is considered to be a function of the slip velocity (v) and of a (or more than one)
465 state variable (θ) as (in the following we consider only a single state variable):

$$466 \mu(v, \theta) = \mu_0 + a \log\left(\frac{v}{v_0}\right) + b \log\left(\frac{v_0 \theta}{d_c}\right) \quad (32)$$

467 In equation 32, μ_0 is a reference friction coefficient corresponding to a reference loading
468 velocity (v_0), the second term describes the so-called „direct effect“, that is, the change in the
469 friction coefficient (weighted by the a parameter) for a sudden change in the loading velocity
470 ($v \neq v_0$). The third term represents the so-called „evolution effect“ exemplifying the memory
471 effect observed in frictional laboratory experiments occurring over a critical distance (d_c),
472 which corresponds to the length over which the frictional resistance evolves after a perturbation.
473 The parameter θ is usually referred to as the state (memory) variable as it characterizes the
474 physical state of the shearing region. There exist different models in terms of the evolution of

475 the state parameters the most used being the aging law by Dieterich (Equation 33a) and the
 476 Ruina slip law (Equation 33b):

$$\begin{aligned}
 & a) \frac{d\theta}{dt} = 1 - \frac{v\theta}{d_c} \\
 & b) \frac{d\theta}{dt} = -\frac{v\theta}{d_c} \log\left(\frac{v\theta}{d_c}\right)
 \end{aligned}
 \tag{33}$$

478 Despite inherent difference in the two formulations, both evolution laws provide the same
 479 steady state asymptotic value for the state variable $\theta_{ss} = \frac{d_c}{v}$. This aspects led to interpret the
 480 state variable as a measure of the characteristic lifetime of the asperity population on the slip
 481 surface the critical distance as a measure of the sliding distance required to establish a new
 482 population of asperity contacts (Lapusta et al., 2000).

483 Equation 30 is a purely empirical formulation of dynamic friction derived as to match available
 484 experimental evidence. The major drawback for its implmentation into a numerical model is
 485 that, by assuming such logarithm formulation the stress has a discontinuity as slip velocity
 486 approaches zero. Therefore, Equation 32 is often regularized as:

$$\mu(\theta, v) = a \sinh^{-1} \left[\frac{v}{2v_0} e^{\left(\frac{\theta}{a}\right)} \right],
 \tag{34}$$

488 The evolution of the state variable is then modified accordingly as:

$$\begin{aligned}
 & a) \frac{d\theta}{dt} = \frac{b v_0}{d_c} \left(e^{\left(\frac{\mu_0 - \theta}{b}\right)} - \frac{v}{v_0} \right) \\
 & b) \frac{d\theta}{dt} = -\frac{v}{d_c} (\mu(\theta, v) - \mu_{ss}) \\
 & \mu_{ss} = \mu_0 + (a - b) \log\left(\frac{v}{v_0}\right)
 \end{aligned}
 \tag{35}$$

490 Within the RSF theory, stick-slip instabilities only arise for certain combination of the a and b
 491 parameter (i.e., $b-a > 0$ == velocity weakening fault, e.g. Rice et al., 2001).

492 A RSF-based simulator was for example developed and applied to fluid injection induced
 493 seismicity problems by Dieterich et al. (2015) and Kroll et al. (2015).

495 **3. Laboratory-scale experiments**

496 Laboratory scale experiments are conducted under well controllable conditions, and thus
497 provide the possibility to reveal how each parameter influences the injection-induced seismicity
498 in geothermal systems by isolating the highly complex coupling among various parameters in
499 the mine and field scales. In this part, the laboratory methods are firstly briefed followed by a
500 summary of laboratory results with some perspectives.

501 **3.1. Laboratory methods**

502 Fault behaviour has been extensively investigated by performing either displacement-driven or
503 injection-driven shear tests. In displacement-driven shear tests, the fault is caused by increasing
504 the shear displacement (e.g., Brace and Byerlee, 1966) or the shear stress (e.g., Cornelio et al.,
505 2020). The fault slip in injection-driven shear tests is caused by introducing fluid pressure into
506 the pre-stressed fault (e.g., Passelegue et al., 2018; Ji and Wu, 2020; Wang et al., 2020).
507 Injection-driven shear tests better simulate injection-induced seismicity in terms of the stress
508 state of the fault and the injection of fluid. There are two main categories of injection-driven
509 shear tests, i.e., fully drained, and locally undrained injection-driven shear tests. In fully drained
510 injection-driven shear tests, the fault slip is induced by uniformly increasing the pore pressure
511 and reducing the effective normal stress on the fault (e.g., Wang et al., 2020). However, the
512 fault slip in locally undrained injection-driven shear tests is probably resulted from the shear
513 stress transfer beyond the pressurized zone (e.g., Ji et al., 2020; Cebry and McLaskey, 2021).
514 From the authors' view, the fully drained condition is more suitable for mimicking small-scale
515 faults with near-uniform fluid pressure distribution, while the locally undrained condition
516 simulates the case of large tectonic faults which can only be perturbed locally by fluid pressure.

517 **3.2. Laboratory results: summary and perspectives**

518 Although the laboratory scale experiments are limited in terms of the scale, some important
519 findings have been reached and significant implications can be drawn out by performing
520 laboratory studies. The displacement-driven shear tests are far more extensively conducted
521 compared to injection-driven shear tests because the former type of shear tests is the
522 conventional approach for seismologists to understand fault behavior underpinning natural
523 earthquakes. Thus, the results obtained from displacement-driven shear tests also lay the
524 foundation for injection-induced earthquakes. Because increasing attention has been paid to
525 injection-induced seismicity in recent years, the number of injection-driven shear tests in the
526 literature keeps increasing, further constraining the underlying processes leading to injection-
527 induced earthquakes.

528 First, fault properties, including fault roughness and mineral composition, appear to be the key
529 controlling factors influencing injection-induced seismicity. The rough fault segment tends to
530 be more aseismic compared to the smooth fault segment in both preparatory and failure stages
531 presumably due to local stress field heterogeneity as revealed by Goebel et al. (2017a) and
532 Dresen et al., (2020). The same trend has also been observed in the injection-driven shear tests,
533 in which the smooth sawcut fault slips dynamically while the rough natural fault slips
534 aseismically (Ji and Wu et al., 2020). From the geology view, a young fault is always rougher
535 compared to a mature fault (Goebel et al. 2017), implying that mature faults can be more
536 dangerous in otherwise similar conditions. Due to the interlocking effect of larger asperities,
537 the friction coefficient and the friction rate parameter (a-b) of rough faults are normally higher
538 than smooth faults (Fang et al., 2018). Compliant minerals, like clay, can weaken the fault by
539 reducing the friction coefficient but can stabilize the fault by increasing the friction rate
540 parameter (a-b) (e.g., Kohli and Zoback 2013; Wang et al., 2019). When it comes to the
541 simultaneous evolution of friction and permeability, the results can be diverse because it is
542 complicated by the coupling among slip rate, surface roughness, normal stress, and mineral
543 composition. Specifically, a higher slip rate tends to increase the fracture aperture and thus

544 increase fault permeability (Ishibashi et al., 2018), but this can also cause more severe asperity
545 damage, which on one hand can reduce the fracture aperture by smoothening the fault, while
546 on the other hand, the shear-off particles can either block the fluid pathway or cause
547 permeability enhancement due to propping effect (e.g., Rutter and Mecklenburgh 2018).
548 Besides, clay swelling in shale rocks can lead to the decoupling among friction and permeability
549 evolution (Fang et al., 2017). Injection-driven fault slip is dependent on the coupling between
550 hydraulic and rate-and-state properties. Hydraulic properties control the fluid migration along
551 the fault, and rate-and-state properties dictate the failure mode of the fault. A velocity-
552 strengthening fault can be induced to slip dynamically by the overwhelming fault weakening
553 included by fluid pressurization (Scuderi et al., 2017). The strong velocity-strengthening shale
554 gouge is induced to slow slip by fluid pressurization due to the periodic fluid migration
555 perpendicular to the fault slip direction and the strong velocity-strengthening of shale gouge
556 prevent the dynamic slip from happening (Scuderi and Collettini et al., 2018). In light of the
557 fault heterogeneity and fluid pressure heterogeneity, we point out that the aseismic-seismic slip
558 transition on a critically stressed heterogeneous fault during fluid injection deserves further
559 investigation.

560 Second, the stress state on a fault determines how much strain energy has been stored in the
561 fault and can also control its injection-induced behaviour mainly by influencing the fluid
562 pressure distribution. It is found that a higher degree of fluid pressure heterogeneity favors
563 larger slip rate (Passuegue et al., 2018) and larger magnitude of seismic moment (Ji and Wu,
564 2020). A higher normal stress reduces the fault aperture and thus the fault permeability. A
565 higher shear stress means a more critically stressed state, allowing insufficient time for fluid to
566 fully diffuse. A faster fluid injection rate promotes the accumulation of fluid around the
567 injection area (Ji et al., 2020). That means, a faster injection rate to a fault under higher
568 magnitudes of deviator stress and normal stress promotes larger magnitude earthquakes by

569 increasing the degree of fluid pressure heterogeneity. Another obvious reason is that a higher
570 magnitude stress state means a higher magnitude of releasable strain energy.

571 Third, high temperature promotes the brittle-ductile transition of rocks and favours the velocity-
572 strengthening behaviour (Scholz 1998). On the contrary, temperature-assisted processes could
573 reduce the reservoir permeability (Polak et al., 2003; Yasuhara et al., 2004) and has the potential
574 to increase the degree of fluid pressure heterogeneity, thus causing larger seismic moment. This
575 means high temperature reservoirs, typically enhanced geothermal systems, suppress the
576 seismic risks by altering rock rheology while increase seismic risks by favouring larger degree
577 of fluid pressure heterogeneity. Thus, the current results suggest our poor understanding on the
578 temperature effects on injection-induced seismicity. In terms of temperature effect, another
579 interesting and meaningful issue remains to be investigated is how a hot and critically stressed
580 fault responds to cold water injection. This could be of great significance to reveal the cooling
581 effect of geothermal reservoirs.

582 Fourth, the effects of fluid physics and chemistry significantly influence the injection-induced
583 seismicity in various ways. The dependence of friction rate parameter (a-b) on pore pressure is
584 debated. It has been reported to increase (Xing et al., 2019) or decrease (Scuderi 2016) with
585 increasing pore pressure. The friction rate parameter (a-b) also reduces with increasing fluid
586 viscosity (Cornelio and Violay, 2020). Because many parameters can influence the evolution
587 of (a-b), we thus suggest measuring the friction rate parameter (a-b) in laboratory experiments
588 under simulated reservoir conditions relevant to operational parameters. The fluid viscosity,
589 among many other fluid physical properties, plays a significant role in controlling fault
590 behavior. Specifically, it can change the macroscopic lubrication regime by changing the
591 Sommerfeld number, altering the fault weakening mechanisms during fault dynamic slip
592 (Cornelio et al., 2019). The fluid chemistry can cause dissolution and precipitation of rocks (Ma
593 et al., 2021), which could also influence injection-induced seismicity. Dissolution potentially

594 increases seismic risks by reducing fault strength (Shang et al., 2020), while the effect of
595 precipitation is two-fold. It can consume fluid volume and distribute the load on fault, reducing
596 seismic risks (Yarushina and Bercovici, 2013). However, the permeability reduction caused by
597 mineral precipitation increases the degree of fluid pressure heterogeneity, increasing the risk of
598 large seismic moment. These results highlight the needs to simulate fluid injection with various
599 viscosities and chemical components into critically stressed faults to shed light on injection-
600 induced seismicity with involvement of fluid properties.

601 Fifth, the injection strategies are the controllable operational parameters, and a well-designed
602 injection strategy has the potential to mitigate seismic risks. The simplest parameter is the
603 injection rate, the effect of which is highly consistent in different studies under undrained or
604 drained conditions. It is demonstrated the faster injection rate promote faster fault slip and
605 thereby increase the seismic risks (e.g., Passelegue et al., 2018; Ji and Wu, 2020; Wang et al.,
606 2020). Apart from the injection rate, the injection protocol is a more comprehensive parameter
607 for investigation. Particularly, cyclic injection protocol has been proposed in recent years and
608 demonstrated as an effective measure to reduce the seismic risks (Hofmann et al., 2018a, 2019;
609 Zang et al., 2013, 2019). However, the laboratory results on cyclic injection obtained under
610 drained and undrained conditions are contradictory. Noel et al. (2020) find that cyclic injection
611 promotes the transition from stable slip to unstable slip by increasing the critical rheological
612 stiffness of the fault. On the contrary, Ji et al., (2021b, 2021c) demonstrate that cyclic injection
613 can reduce the fault slip rate and seismic moment by reducing the degree of fluid pressure
614 heterogeneity. Therefore, investigating the friction evolution of fault during cyclic injection
615 under drained and undrained conditions can help to reconcile these two opposite findings.

616 **4. Mine-scale experiments**

617 Limitations of fluid-injection experiments in the laboratory result from the finite sample size
618 and related boundary effects. For example, the dynamic rupture and/or shearing process via
619 fluid injection into rock cannot be studied in terms of the energy budget involved in the rupture
620 process since the growth path and segmented fault slip patches (asperities) are not to scale
621 compared with complex fault zone architecture in nature (Zang et al., 2021). One can think of
622 solving this problem in two ways. One can increase the size of laboratory samples to several
623 meters (e.g., Cebry and McLaskey, 2021), and one can perform underground decameter-scale
624 in-situ experiments (e.g., Gischig et al., 2020; Zang et al., 2017). Below, we focus on reviewing
625 mine-scale experiments to understand and control the mechanisms of fluid-injection-induced
626 seismicity. We distinguish between stimulation tests with focus on hydraulic fracturing (4.1),
627 and stimulation tests aiming at fault reactivation by injecting fluids (4.2). Underground tests in
628 naturally fractured rock mass have the advantage that mechanical and hydraulic discontinuities
629 and in-situ stress conditions are taken into account while only one parameter is changed at a
630 time (e.g., injection style). The natural rock mass response is monitored using complementary
631 sensor arrays (acoustic emission, borehole geophones, fibre optics (acoustic, strain, pressure)
632 and electro-magnetic sensors). The accurate observation and detailed analysis of such in-situ
633 fluid-injection experiments with the aid of advanced instruments provides fruitful insights into
634 how fluid pressure migrates in naturally fractured rock mass, how seismic and aseismic
635 deformation and motion of the fault is induced, and how these coupled processes interact.

636 **4.1. Mine-scale hydraulic fracturing (and shearing) experiments**

637 In this section, we review in-situ experiments performed at three European and one US
638 underground test facility for geothermal purposes. According to the depth of the decamter
639 stimulation tests in hard rock, we distinguish between Äspö Hard Rock Laboratory, Sweden
640 (depth level 410 m; Zang et al. 2017), the Grimsel Test Site, Switzerland (480 m; Amann et al.

641 2018), Bedretto Underground Laboratory, Switzerland (1200 m below the topography of the
642 Aar massive; Gischig et al 2020), and the Sanford Underground Facility in Lead, South Dakota
643 USA (1480 m; Kneafsey et al. 2018) formerly known as Homestake Gold Mine. The interesting
644 element tested at Äspö HRL, was the concept of hydraulic fatigue in generating multiple
645 geothermal heat exchanging surfaces at depth in a stimulated rock volume of 30x30x30 cubic
646 meter in size. Zang et al. (2019) found that cyclic and pulse-pressurization of intact granitic
647 rock mass stimulated with 30 liter of water from a dedicated horizontal injection borehole (28
648 m long) and three 30-m long inclined monitoring boreholes allow to control (a) the ratio of
649 seismic radiated and hydraulic energy, (b) the permeability enhancement process, and (c) the
650 evolution of the fracture network documented in acoustic emission hypocenters and impression
651 packer results. In particular, in the early stimulation phase the injection style can help to modify
652 the seismic event distribution towards higher seismic b -values which indicates a safer treatment.
653 Pressure pulses applied with a secondary pump allow for generation of more complex fracture
654 pattern most probably resulting from natural rock proppants as confirmed by accompanying
655 laboratory hydraulic fracturing experiments (Zhuang et al. 2020). The treatment with combined
656 cyclic injection and pressure pulses lead to the best permeability enhancement in diorite gabbro.
657 At the moment, we see three limitations of the hydraulic fatigue concept. First, there is
658 optimization potential in finding tailored injection strategies, i.e. reducing seismic impact while
659 preserving the permeability enhancement process for different rock types. Second, fatiguing the
660 rock at later times in the reservoir life-time, i.e. circulation of fluids during production, may not
661 be different from using conventional stimulation methods. Third, if the hydraulic stimulation
662 process and the fracture network generated or activated starts to interact with larger-scale
663 hidden tectonic faults, hydraulic fatigue like any other method cannot prevent runaway fractures
664 (Lyakhovsky and Shalev 2021, Bentz et al. 2020, Woo et al. 2019, Zang et al. 2014).

665 Interesting findings from the Grimsel Test Site hydraulic fracturing (HF) and hydraulic shearing
666 (HS) experiments are the following. Comparison of deformation and pressure monitoring data

667 within the foliated rock mass and the location of microseismic events suggests that the
668 activation of seismic events lags slightly behind the propagation of the pressure front (Dutlet et
669 al. 2019). Using acoustic televiewer logging, the maximum induced cumulative slip was
670 estimated ~ 1 mm for individual experiments with 1 m³ of fluid injected (Krietsch 2019). During
671 HS it was found that pressure perturbations were usually 10% of the injection pressure value.
672 However, in few tests pressure perturbations reach 80% of the initial pressure. This indicates
673 pressure channels along shear target structures (Krietsch et al. 2020). Close to the injection
674 interval, deformation monitoring indicates rather complex fracturing processes (tensile, shear
675 and mixed mode wing-cracks). Further away from the injection interval, the deformation system
676 indicated volumetric compression. This division into primary (inner) and secondary (outer)
677 stimulated volume is consistent with observation from 3D seismic tomography (Doetsch et al.
678 2018) and is consistent with near-field and far-field analysis results of fracture modes from
679 microseismic field studies in EGS systems (Zang et al. 2014, Preface Geothermics). In
680 summary, two fundamental deformation mechanism are observed at Grimsel: (a) static, shear-
681 induced stress transfer in the near-field, and (b) dynamic, poroelastic stress transfer further
682 away from the injection interval. A limitation at Grimsel test site was that the rock mass
683 response for HF and HS experiments were not clearly distinguishable because HF and HS tests
684 both interact with the same pre-existing fracture system at depth (Villinger et al. 2019).

685 At Sanford Underground Research Facility (Lead, ND USA), a testbed consisting of eight 60-
686 m length monitoring boreholes was designed to study the creation and function of a subsurface
687 heat exchanger based on the utilization of hydraulic fracture designed to connect an injection-
688 production borehole doublet. Hydraulic fracturing and shear stimulation experiments were
689 performed at 1480 m depth below surface. Three intervals of the dedicated injection borehole
690 were hydraulically stimulated by water injection at pressures up to 33 MPa and flow rates of 5
691 liter/minute with 1933 seismic events recorded during several injection periods (Schoenball et
692 al. 2020). Stress heterogeneity in the strongly foliated metamorphic rock is found to dictate the

693 seismic outcome of the hydraulic stimulations. In order to create an efficient subsurface heat
694 exchanger, it is suggested that production boreholes should not be drilled before the end of
695 hydraulic stimulations. In my opinion, an interesting outcome of the second, the 43-m borehole
696 depth test was that the rock volume forced to hydraulic fracturing was responding in hydraulic
697 shearing. Also, two re-stimulations with notched interval and with loss of one packer system
698 could not prevent the upper Poorman formation from hydro-shearing. One has to have a clear
699 understanding of the stressed rock mass stimulated to forecast its behaviour during injection of
700 high-pressurized fluids. Another interesting outcome of this project is the idea of using fracture
701 caging to limit induced seismicity (Frash et al. 2021). Although fracture caging is not a new
702 concept (Weijermars et al. 2012), the application in the geothermal context to limit seismic
703 radiated energy is worth to be investigated. The basic idea of fracture caging is to drill extra
704 production wells which can impede fracture growth and contain high-pressure fluid in fracture-
705 dominated rock. This containment offers a mechanism to limit induced seismicity in EGS
706 development. A limitation of fracture caging is that if the flow sinks cannot cage the high-
707 pressurized fluid, tectonic faults can be activated. Like a fire accelerant, the caged volume if
708 vented can cause runaway fractures, too. A second, economic drawback is that drilling four
709 extra boreholes for caging purposes is costly.

710 **4.2. Mine-scale fault re-activation experiments**

711 Fluid injection experiments on decameter scale (10 m) faults in the field bridge the gap between
712 centimeter scale (cm) laboratory experiments and kilometer scale (km) geothermal systems.
713 The accurate observation and detailed analysis of fluid injection experiments in decameter scale
714 with the aid of advanced instruments could provide fruitful insights into how fluid pressure
715 migrates, how seismic/aseismic deformation/motion of the fault is induced, and how these
716 coupled processes interact.

717 The apparatus and injection protocols used in field fluid injection experiments on in-situ faults
718 are detailed shown in Guglielmi et al., (2015a). A three-dimensional deformation unit is
719 employed to measure the displacement field of the fault, which can be resolved as the shear and
720 normal displacements. Water is injected through a borehole into an injection chamber isolated
721 by two inflatable packers. The injection flow rate, injection pressure and in-situ temperature are
722 also recorded. A concurrent measurement of these shear-flow characteristics of the fault can be
723 achieved through these efforts (Guglielmi et al., 2015a). Several field fluid injection
724 experiments have been performed on faults intersecting limestones in the low-noise laboratory
725 Laboratoire Souterrain à Bas Bruit (LSBB) of Rustrel, southeast France (De Barros et al., 2018;
726 Derode et al., 2015; Duboeuf et al., 2017; Guglielmi et al., 2015b), shales in Tournemire URL,
727 Southern France (De Barros et al., 2016; Guglielmi et al., 2015a), and clay in Mont Terri
728 Underground Research Laboratory (URL), Switzerland (Jeanne et al., 2017, 2018).

729 In combination with laboratory experiments (Cappa et al., 2019) and numerical modelling
730 (Bhattacharya and Viesca, 2019; Cappa et al., 2018; Cappa et al., 2019; Guglielmi et al., 2015b,
731 2015b; Jeanne et al., 2018; Kakurina et al., 2019), insightful findings are reached from these
732 fluid injection experiments on in-situ faults. Some general insights are summarized here.

733 1) The interplay among fluid pressure build-up and diffusion, fault normal and shear
734 deformation, as well as fault permeability change are complex during field fluid injection
735 experiments on in-situ faults. Particularly, the fault deformation is controlled by the fault
736 complexities (Guglielmi et al., 2020). The heterogeneous stress response to fluid injection
737 resulted from the structural heterogeneity causes the complex seismic/aseismic response of
738 fault, because of the frictional heterogeneity of the fault (De Barros et al., 2016; Guglielmi et
739 al., 2015b).

740 2) Fluid injection often directly induces aseismic slip of velocity-strengthening fault segments,
741 which then triggers seismic slip of unpressurized fault segments. This happens because of the

742 accumulated shear stress caused by propagating aseismic slip in the unpressurized area (stress
743 transfer), where the fault segment is velocity-weakening (Cappa et al., 2018; Cappa et al., 2019;
744 Guglielmi et al., 2015b). The permeability changes in the reactivated fault patches are
745 heterogeneous (Cappa et al., 2018; Guglielmi et al., 2015a; Jeanne et al., 2018), while an overall
746 permeability increase is the necessity for accumulating shear stress beyond the pressurized zone
747 (Cappa et al., 2018).

748 3) The occurrence of seismic events can be independent of fluid diffusion, which is found to be
749 caused by stress perturbation resulted from aseismic motion (De Barros et al., 2018; Duboeuf
750 et al., 2017). Aseismic deformation can be a major pattern of injection-induced strain energy
751 release on faults (De Barros et al., 2016; Duboeuf et al., 2017; Guglielmi et al., 2015b). In other
752 words, the release of injection-induced seismic moment can be accommodated by aseismic slip
753 within and beyond the pressurized zone. Therefore, the current prediction of maximum seismic
754 moment based on injection-induced stress change (McGarr, 2014) and stimulated reservoir
755 volume (Shapiro et al., 2011) may overestimate the maximum magnitude of injection-induced
756 earthquake in some cases.

757 **5. Field-scale induced seismicity**

758 Here, the characteristics of induced seismicity at specific geothermal sites are evaluated with
759 respect to stress perturbations caused by cold water injection. The geothermal sites are
760 compared to three reference sites, where induced seismicity was caused by different (from
761 geothermal) human activities like chemical waste disposal (Denver CO, USA), on-land gas
762 exploitation (Groningen, NL) and massive hydraulic injection tests in two scientific wells
763 (KTB, Germany). While the European sites are located near or over densely populated areas,
764 all other sites are located in remote areas.

765 **5.1. Hydrothermal systems**

766 Paris Basin (France)

767 In the Paris Basin 34 geothermal doublets are in operation and no induced seismicity was
768 observed. Buijze et al. (2020) speculate that thick sequences of shales between the carbonate
769 reservoir and the crystalline basement could have prevented pressure and temperature
770 perturbations extending to depth. Thus, the local lithology together with the operational
771 parameters and in situ stress may explain why no seismicity was observed in any of the 34
772 doublets.

773 The Geysers CA (USA), see Majer et al. (2007). The Geysers site is characterized by an
774 extensional tectonic setting with local reservoir contraction due to injection-induced cooling.
775 Little seismicity occurred prior to the 1960 start-up of the commercial production of this high
776 temperature geothermal system. Induced seismicity has been generated by geothermal activity.
777 Since 1980 three events with $M_L > 4$ and 18 with $M_L > 3$ occurred. 1982 a $M_L = 4.6$ event was
778 detected, and in 2006 three $M_L > 4$ events occurred. Maximum event size depends on the size of
779 fault available for slippage, and the stress perturbation caused by the change in fluid volume
780 injected or withdrawn from the reservoir. Due to the absence of continuous long faults,

781 maximum LME is estimated to be $M_L < 5$ at the site. Induced seismicity is generally below
782 magnitude 3, since 1989 the SE Geysers area has experienced a long-term increase of $M > 1.5$
783 magnitude events. In late 1997, injection rates in the SE Geysers area doubled, producing
784 minimum one event per day on average which is felt by the residents (Majer et al. 2007).
785 Shallow earthquakes induced by steam production are caused by poroelastic stress transfer
786 during pressure depletion of the underlying reservoir (Rutqvist et al. 2006), whereas deep
787 production induced seismicity is explained by thermoelastic stresses resulting from evaporate
788 cooling. The mechanism discussed is cooling-induced shear slippage along pre-existing
789 fractures associated with thermo-elastic shrinkage. Rutqvist and Oldenburg (2007) studied
790 mechanisms of induced seismicity using coupled thermal-hydrological-mechanical modeling
791 at two temporal scales: analysis of 44 years of production (1960-2004) and seasonal injection
792 cycles (2004-2005). Applying Coulomb's failure criterion with 30° friction angle results in rock
793 failure, if changes in maximum principal stress exceed 3 times the changes in minimum
794 principal stress at the site. Both, modeling and observation (Stark, 2003) show that most of the
795 injection induced seismicity occurs near the injection and production wells. Shear slip along
796 existing fractures as a result of reduced minimum principal compressive stress is the most likely
797 mechanism of induced-seismicity at The Geysers. Near production wells, thermo-elastic
798 cooling shrinkage due to evaporate cooling is the dominant causes for stress perturbations
799 leading to injection-induced seismicity. Near injection wells at greater depth, both thermo-
800 elastic cooling and elevated fluid pressure contribute to reducing the effective stress producing
801 microquakes.

802 **5.2. Enhanced Geothermal Systems**

803 Soultz-sous-Forêt (France). The geothermal reservoir located in the Upper Rhine Valley is
804 accessed by four boreholes in different operational phases (GPK1, depth $z = 2002$ m, bottom
805 hole temperature $T = 140^\circ$, year 1987), (GPK1, $z = 3590$ m, $T = 160^\circ$, 1992), (GPK2, $z = 3890$ m,

806 1995), (GPK2, $z=5084$ m, $T=202^\circ$, 1999), (GPK3, $z= 5000$ m, 2003) and (GPK4, $z=5260$ m,
807 2004). Stimulation of GPK2 in 2000 with $23,000$ m³ of water injected with a rate of up to 50
808 L/s produced a large magnitude event (LME) with $M_w =2.4$ seven days later. Stimulation of
809 GPK3 in 2003 with $37,000$ m³ water injected into the reservoir at a rate of up to 80 L/s over
810 eleven days produced a LME $M_w =2.9$ about two days after shut-in. GPK4 has been stimulated
811 twice (2004, 2005) by injecting a total volume of $22,000$ m³. Based on induced seismicity
812 hypocenters observed (Cuneot et al. 2008), a single, large scale fault (fracture zone) of tectonic
813 origin (Rhine Graben structure) is assumed at the Soultz geothermal reservoir.

814 Baisch et al (2010) used a block-spring model to simulate the reservoir. Mechanically coupled
815 patches (20x20 m in size) extend over the planar reservoir structure (20x20 km in size) with
816 constant pressure boundaries. The physical process of rock fracture is approximated by slippage
817 of blocks controlled by Coulomb friction with constant stress drop. Dynamic stress transfer to
818 neighboring blocks results in avalanche fractures, where the event magnitude is determined by
819 the slip area, i.e. the number of block patches slipping simultaneously. This simple model
820 matches zero-order observations at Soultz, such as hydraulic overpressures, the spatiotemporal
821 distribution of injection-induced seismicity, event rates and magnitudes, as well as the
822 occurrence of LME post-injected seismicity. 114,000 seismic events were detected during
823 stimulation of the three wells with a local seismic network of accelerometers and geophones at
824 1.5 to 3.5 km observation depth. Seismicity observed supports a single, subvertical aligned
825 planar structure. Interaction of fault patches is controlled by (1) stress transfer, and (2) stress
826 drop. With increasing stress drop, the maximum LME increases while the total number of
827 induced seismicity events decreases. The location of seismic activity migrates away from the
828 injection well when the injection pressure remains constant. LME occur in the post-injection
829 period, and are attributed to a geometrical effect.

830 Basel (Switzerland). This geothermal reservoir is located under the city of Basel in a high-stress
831 region ($S_H > S_V > S_h$) associated with the historical 1356 earthquake $M > 6.5$. Stimulation of well

832 Basel 1 in 2006 with 11,570 m³ of Rhein river water at rates up to 62 Liter/s produced six days
833 later a LME with local magnitude 3.4. The mechanism of the induced seismicity observed is a
834 hydraulically induced shearing process. The reservoir fracture system developed parallel to the
835 maximum horizontal stress (N144°E±14°) in a pre-existing, cataclastic fracture zone (Häring
836 et al. 2008). Between December 2006 and March 2007, six borehole seismometers recorded
837 more than 13,500 induced seismicity events. The 200 largest between local magnitudes 0.7 and
838 3.4 (Deichmann & Giardini 2007). Focal mechanisms of the 28 strongest events, with
839 magnitudes M_L between 1.7 and 3.4, have been analyzed (Deichmann & Ernst 2009). Except
840 for two normal faulting events, all other solutions indicate strike slip faulting mechanisms with
841 P -axis N138°E±13° oriented almost parallel to the maximum horizontal compression stress in
842 the reservoir. The largest magnitude event occurred during the shut-in period, which is
843 attributed to continued pressure diffusion even after shut-in.

844 Berlin (El Salvador) is an EGS on the margins of a producing field. Natural background
845 seismicity is caused by subduction of the Cocos plate (moment magnitude $M_w=7$ in 2001), and
846 shallow earthquakes are due to Quarternary volcanoes ($M_w =6.6$ in 2001). Berlin is a fracture-
847 dominated geothermal field in which only seismically active faults remain permeable. A traffic
848 light system based on peak ground velocity thresholds has been implemented to control induced
849 seismicity vibrations. Cumulative moment release of induced seismic events around the
850 injection well show a remarkable correlation with the cumulative pumped volume of injections
851 (Majer et al. 2007).

852 Cooper Basin (Australia) is a geothermal resource in a sparsely populated region. The total
853 amount of 20,000 m³ water injected to a hot zone of Habanero 1 granites (perforated casing
854 between 3994 and 4136 m) with a maximum pumping rate of 48 Liter/s in 2003 produced a M_w
855 =3.7 LME (Baisch et al. 2006). LME occur at the edge of the induced seismicity cloud.
856 Previously activated regions become seismically quiet (Kaiser memory), indicating a relaxation
857 process. High resolution, relative induced seismicity hypocenters provide evidence for a single-

858 fracture geothermal reservoir. Mechanisms of LME and small EQ at the site are similar and
859 explained by induced slip on pre-existing, sub-horizontal fractures. The size of the breaking
860 asperities along the fracture ligaments correlates with the moment magnitude of induced events.
861 Prior to LME, stressed asperities block permeability channels. The fact that LME occur after
862 shut-in support the theory that the initial stress state was critical. There is no distinct change in
863 wellhead pressure associated with LME (Majer et al. 2007).

864 A second fluid-injection experiment was carried out in 2005 to enlarge the reservoir in the
865 Cooper Basin. 25,000 m³ of water were injected at 4250 m depth triggered 16,000 seismic
866 events recorded at eight local stations resulting in 8886 hypocenters located (Baisch et al. 2009).
867 In the re-stimulation experiment the onset of induced seismicity was delayed by 22 hours. The
868 2005 seismicity hypocenters occur at the NE fringe of the region from the 2003 seismic
869 hypocenters, and migrate back to the injection well. The seismic zone of quiescence near the
870 injection well is interpreted by the Kaiser effect (no seismic events in re-stimulation before the
871 maximum fluid pressure from the first stimulation has been reached). Baisch et al. (2009)
872 conclude that induced seismicity is primarily controlled by fluid overpressures rather than by
873 Coulomb stress transfer.

874 **5.3. Reference Sites**

875 The following sites have been chosen, because of different reasons. First, an end-member
876 scenario in fluid volume injected into the Earth's crust was carried out near Denver, Colorado.
877 Second, induced seismicity caused by gas exploitation was observed and analyzed at
878 Groningen, NL. Third induced seismicity associated with massive hydraulic tests in a non-
879 geothermal, crystalline basement area (KTB, Germany).

880 Denver CO (USA). In 1961 a deep disposal well (depth 3671 m) was completed for the US
881 Army at the Rocky Mountain Arsenal, NE of Denver, Colorado. The injection of chemical
882 waste fluids in the well began March 1962 at rates 3 to 8 Liter/s and lasted (with interruptions)

883 until Feb. 1966 because of a suggested connection between fluid injection and earthquakes in
884 the Denver area. About 650,000,000 m³ of waste fluid were pumped into the subsurface. 1967
885 three LME occurred with magnitude between 5 and 5.5. The energy released by the EQ was
886 stored in the crystalline basement rocks (overlaid by 3638 m of nearly flat-laying sedimentary
887 rocks in the Denver basin) as nonhydrostatic elastic strain. EQs are produced by the tectonic
888 stress field. According to the Healy et al. (1968) model based on Hubbert & Rubey (1959), the
889 effect of increasing pore pressure is to reduce the frictional resistance to fracture by decreasing
890 the effective normal stress across the fracture plane (21 MPa). Hydraulic fracturing and slip on
891 pre-existing faults has been discussed as mechanisms for induced seismicity caused by pore
892 pressure increase. The Denver earthquakes are one exception from the unwritten rule that
893 magnitudes of induced seismicity never reach values higher compared to the magnitude of
894 natural seismicity in the area of interest before any interaction of human beings with the Earth`s
895 crust.

896 Groningen (NL), see van Eck et al. (2006). Seismicity in S-NL is related to the Roer Valley
897 graben and of tectonic origin. Seismicity in N-NL is induced by gas exploitation and is mainly
898 caused by the reactivation of existing faults (Roest and Kuilman 1994). Groningen reservoir is
899 situated in the sandstones of the Upper Rotliegend at depth from 2600-3150 m. The first event
900 occurred 1991, 28 years after the gas production started. From 1991-2003, 179 induced
901 seismicity events were identified in the magnitude range $-0.2 < M_L < 3$. Many events occur along
902 NW-SE trending faults at the reservoir level. LME in Roswinkel and Bergermeer field were
903 $M_L=3.4$ and $M_L =3.5$, respectively. Seismicity in Roswinkel occurs above the reservoir
904 sandstones (2000-2400 m) in an anticline salt structure. Seismicity in Bergermeer is associated
905 with re-activation of one major normal fault. Maximum LME in N-NL is unlikely to exceed M_L
906 $=3.9$ (van Eck et al. 2006).

907 Induced seismicity from hydrocarbon exploitation is a result of slip on pre-existing surfaces
908 (Grasso 1992, Segall et al. 1994). Slip is induced by poroelastic stress changes in the reservoir

909 and surrounding rocks. This can be caused by fluid injection (Healy et al. 1968), fluid extraction
910 (Segall and Fitzgerald 1998), and poroelastic stress transfer (Segall 1989). Other mechanisms
911 discussed are mass transfer (McGarr 1991) and stress as well as pore pressure diffusion (Grasso
912 1992). Elastic rock properties play an important role in stress development along faults during
913 hydrocarbon production (van Eijs et al. 2006).

914 Van Eijs et al. (2006) determined three key parameters to explain the induced seismicity events
915 associated with gas production in the N-NL. These parameters include the pressure drop in the
916 reservoir, fault density at the site, and the ratio between the Young's modulus of the seal rock
917 and the Young's modulus of the reservoir rock. Based on the observed correlation between the
918 key parameters and the seismicity, a Bayesian probability has been calculated for the occurrence
919 of induced seismicity in field with and without natural seismicity recorded previously.

920 According to van Eijs et al. (2006), only 16 out of 124 producing hydrocarbon fields in NL
921 have shown associated seismicity. The pressure drop of the first induced seismicity quake
922 ranges from 11 to 51 MPa. For Groningen, the value is 20 MPa resulting in a $M_L = 2.4$ EQ in
923 1991. This is comparable to the Denver value (21 MPa), indicating that the initial in-situ stress
924 is critical to know and not listed in Table 2 of van Eijs et al. (2006). For stiffness ratios $S < 1.2$
925 and fault density values $F < 1.2$ no seismic energy release is observed. Note that van Eijs et al.
926 (2006) are able to estimate the probability of induced seismicity in gas exploitation fields even
927 if no natural seismicity was observed before the time of human intervention.

928 KTB (Germany), see Zang and Stephansson (2010). The 1994 short-term (24 hours) fluid-
929 injection test at 9.1 km depth in the KTB-HB produced about 400 microquakes. A total of 200
930 m³ of heavy brine was injected into the ~70 m open hole section near the bottom of KTB-HB
931 at rates of up to 10 Liter/s (Zoback & Harjes 1997, Jost et al. 1998). Seismicity during the
932 experiment was monitored by one borehole sonde in the KTB-VB at about 4 km depth and 73
933 surface, short-period seismometers. Seismicity was located maximum 100 m away from the

934 hole, and only above 9.1 km depth with magnitudes smaller than $M = 1.2$. Most fluid-induced
935 microquakes had a strike-slip faulting mechanism with NNW trending P axis (Zoback & Harjes
936 1997) assumed to align parallel to the maximum horizontal compressive stress at the drill site.
937 Since very small (≤ 1 MPa) pore pressure perturbations were found to trigger induced
938 seismicity, Zoback and Harjes (1997) concluded that Byerlee's law ruling the coefficient of
939 sliding friction is valid to 9.1 km depth and that the continental crust at KTB is critically
940 stressed.

941 The 2000 long-term (60 days) fluid-injection test in the well KTB-HB was hampered by a
942 casing leakage at about 5.4 km depth (Baisch et al. 2002). A surface seismic network consisting
943 of 39 three-component seismometers and one borehole seismometer at 3827 m depth in the well
944 KTB-VB (yielding a low magnitude threshold $M_{w} = -2.5$ for events, Bohnhoff et al. (2004)) was
945 used to map 2800 induced events over three months duration including the injection period.
946 During the injection phase, 4000 m³ fresh water were pumped over a period of 60 days at flow
947 rates between 30 and 70 l/min in the KTB-HB. Bohnhoff et al. (2004) found dominating strike-
948 slip faulting mechanisms with inferred maximum principal stress direction oriented N-S ± 15
949 degrees by analyzing 125 fault plane solutions from the 2000 fluid-induced seismicity events.

950 Triggering mechanisms of fluid-induced seismicity at KTB are discussed by Baisch and Harjes
951 (2003) and Rothert et al. (2003) based on the model suggested by Healy et al. (1968). Fluid-
952 induced seismicity occurs at fractures where elevated pore pressures exceed the critical value
953 to cause Coulomb failure. Baisch and Harjes (2003) assume the Healy model valid at KTB
954 because (1) moment tensor orientations are consistent with the orientation of the local in-situ
955 stress field from the integrated stress approach, and (2) repeating events (seismic multiplets)
956 show hypocenter locations generated from the same fault plane. Hypocenters of the 2000 fluid
957 injection test were found to group along the fringe of induced events located after the 1994 fluid
958 injection test (Baisch et al. 2002). Most of the hydraulic energy induced (10^{11} J) is converted

959 into potential energy to rise the ground-water level at KTB; only a small fraction is converted
960 into seismic energy (10^8 J), as pointed out by Baisch and Harjes (2003). They therefore argue
961 that the fracture network is able to memorize the previous maximum fluid pressure it has
962 experienced during the field test (Kaiser effect). Crustal memory indicates that shear stress
963 relaxations caused by fluid injection in a tectonically passive region such as KTB persisted for
964 at least six years (1994-2000).

965 The result of the one-year production test (2002-2003) and the 10-months injection test (2004-
966 2005) are summarized in Kümpel et al. (2006). During the 10-months injection test, a total of
967 84,600 m³ of fresh water was pumped into the open hole section of KTB-VB. About 3000 fluid-
968 induced seismic events were detected by the borehole seismometer and 150 events were located
969 by the local seismic surface network (Shapiro et al. 2006). Seismicity started only after injecting
970 a fluid volume approximately equivalent to the amount previously extracted (Kaiser effect).
971 The crystalline crust at KTB was mechanically stable when pore pressure was reduced below
972 its natural level by the production test, but became instable (producing earthquakes) when small
973 (~ 0.1 to 1 MPa) positive pore-pressure perturbations were created by the fluid injection test.

974

975 **6. Discussion**

976 **6.1. Key parameters and processes governing induced seismicity**

977 **6.1.1. Processes**

978 **Poro- and thermoelasticity**

979 Thermal stresses play an important role in the seismic hazard in vapour-dominated geothermal
980 systems such as the Geysir geothermal field. Their role in low-to-medium enthalpy geothermal
981 plays, such as the Paris basin or the North German Basin, is still a subject of an ongoing debate.

982 The stress strain relation of a porous poroelastic medium can be written in matrix form as
983 follows (according to Zimmerman, 2000):

984
$$\varepsilon = \frac{1}{2G} \sigma - \frac{\nu}{2G(1+\nu)} \text{trace}(\sigma) \mathbf{I} - \frac{\alpha}{3K} P_p \mathbf{I} \quad (36)$$

985 with strain tensor ε , stress tensor τ , shear modulus G , Poisson ratio ν , Biot coefficient α , pore
986 pressure P_p and unit matrix \mathbf{I} . Taking the trace leads to:

987
$$\varepsilon_b = \text{trace}(\varepsilon) = \frac{1}{K} (P_c - \alpha P_p) \quad (37)$$

988 with confining pressure P_c , which is the isotropic part of the stress tensor.

989 Including (37) in (36) leads to

990
$$\sigma - \alpha P_p \mathbf{I} = 2 G \varepsilon + \lambda \text{trace}(\varepsilon) \mathbf{I} \quad (38)$$

991 With the Lamé parameter λ .

992 The thermal strain is defined as (Zimmerman, 2000):

993
$$\varepsilon = -\beta (T - T_0) \mathbf{I} \quad (39)$$

994 With linear thermal expansion coefficient β and $\Delta T = (T - T_0)$ temperature change.

995 From the basic assumption of linearised thermoelasticity, a rock is subject to both temperature
 996 and applied stress state, then the resulting strain is the sum of thermal strain and stress induced
 997 strain (Zimmerman, 2000):

$$998 \quad \varepsilon = \frac{1}{2G} \sigma - \frac{\nu}{2G(1+\nu)} \text{trace}(\tau) \mathbf{I} - \beta (T - T_0) \mathbf{I} \quad (40)$$

999 Taking the trace of both sides lead to:

$$1000 \quad \varepsilon_b = \text{trace}(\varepsilon) = \frac{P_c}{K} - 3\beta (T - T_0) \quad (41)$$

1001 With 3β the volumetric thermal expansion coefficient.

1002 Combining (40) and (41) leads to the equation of stresses in terms of strains:

$$1003 \quad \sigma = 2G\varepsilon + \lambda \text{trace}(\varepsilon) \mathbf{I} - 3\beta K (T - T_0) \mathbf{I} \quad (42)$$

1004 We can now quantify the relative size of thermoelastic and poroelastic stresses due to pressure
 1005 and temperature changes. Thermal stress change $\Delta\sigma_T$ due to temperature change $\Delta T = (T - T_0)$
 1006 is described in (42) by the term:

$$1007 \quad \Delta\sigma_T = 3\beta K (T - T_0) \quad (43)$$

1008 The poroelastic stress change $\Delta\tau_P$ due to pore pressure change ΔP is described in (38) by the
 1009 term:

$$1010 \quad \Delta\sigma_P = \alpha \Delta P \quad (44)$$

1011 From both equations (43) and (44) the ratio between thermoelastic ($\Delta\tau_T$) and poroelastic stress
 1012 changes ($\Delta\tau_P$) can be obtained (e.g. Segall & Fitzgerald, 1998 (with corrected factor 3);
 1013 Hassanzadegan et al., 2011):

$$1014 \quad \frac{\Delta\sigma_T}{\Delta\sigma_P} = \frac{3\beta K \Delta T}{\alpha \Delta P} \quad (45)$$

1015 Depending on the temperature changes due to cold water injection, thermal stresses can exceed
1016 the poroelastic stresses due to pressure changes by fluid injection (Figure 4). In Table 2 the
1017 thermoelastic and poroelastic parameters for Flechtinger sandstone (Hassanzadegan et al.,
1018 2012), Upper Jurassic Malm limestone (Pei et al., 2018; 2020) and Westerly granite
1019 (Zimmerman, 2000; Wong & Brace, 1979) are summarized.

1020 The results show that the thermal stress cannot be neglected during typical hydrothermal
1021 reservoir conditions with pressure changes below 5 MPa and temperature changes of more than
1022 20°C. For geothermal use a typical injection temperature is up to 100°C lower than the
1023 formation temperature. In this case the thermoelastic stress is more than 10 times larger as the
1024 poroelastic stress (Figure 4).

1025 During stimulation treatments, the pressure is often temporarily increased by more than 50 MPa
1026 and the injection temperature is typically ~20°C. Depending on the reservoir temperature,
1027 temperature changes often more than 100°C. In this case also thermoelastic stress is exceeding
1028 the poroelastic stress.

1029 The results for Malm limestone and Westerly granite are similar (not shown), since the
1030 properties like linear thermal expansion coefficient, saturated bulk modulus and Biot's
1031 coefficient are not very different to Flechtinger sandstone.

1032 **Changes in frictional properties due to chemical processes**

1033 Re-injection of cold reservoir fluid or stimulation using surface water often alter the chemical
1034 equilibrium in a geothermal reservoir. Processes such as the hydrolysis or dissolution of quartz
1035 (Rimstidt and Barnes, 1980) and plagioclase (Gudbrandsson et al., 2014) may lead to a
1036 reduction of fault friction coefficient and thus may trigger failure. Dissolution of fault asperities
1037 may lead to strengthening of a fault in chemical equilibrium conditions by reprecipitation
1038 around the dissolved asperities and thus increasing the fault contact area (Yasuhara et al., 2005).

1039 In unequibrated conditions, without reprecipitation, asperity solution may reduce this contact
1040 area, thus reducing the effective normal stress and “unclamping the fault”. Such a mechanism
1041 has for example been explored for the Pohang EGS system by Westaway and Burnside (2019).

1042 **Aseismic slip**

1043 It has been recognised that injection induced moment release can also be aseismic (McGarr and
1044 Barbour, 2018) and that aseismic slip in pressurized regions of a fault can activate slip along
1045 nonpressurized fault patches (Guglielmi et al., 2015a; De Barros et al., 2018; Cappa et al., 2019;
1046 Morel et al., 2020). Eyre et al. (2019) propose that distant dynamic (seismic) slip of faults may
1047 have been initiated when the creep front from stable sliding (aseismic slip) on a fault patch with
1048 slip rate strengthening properties reaches a region on a fault where its composition favours
1049 dynamic slip rate weakening behaviour in a hydraulic fracturing site in central Alberta, Canada.

1050 **6.1.2. Geological parameters**

1051 Critically stressed faults, that is, faults that are close to failure in the local stress field, can be
1052 reactivated by very small stress or pressure changes that exceed natural variations (i.e. earth
1053 tides) in the order of >0.05 MPa (Cochran et al., 2004). It is generally accepted that the largest
1054 possible seismic event size of a specific area is constrained by the size of the largest fault. When
1055 only small-scale fracture systems are present and no large-scale faults, seismicity typically does
1056 not occur beyond the volume perturbed by geothermal operations and shear slip may be
1057 considered as stable. Unstable runaway fault slip triggered by small perturbations may only
1058 occur when large faults are present. Besides the stress field, also the frictional properties of the
1059 fault are important for the local seismic risk. Also, the influence of poroelastic and thermoelastic
1060 stress changes strongly depends on the elastic moduli of the local geological units.

1061 Overall, structural heterogeneities, including heterogeneous frictional properties, cause a
1062 complex seismic and aseismic response of a fault to perturbations induced by geothermal

1063 reservoir operations. Current knowledge suggests that the influence of geological parameters
1064 such as the presence of large critically stressed faults can be considered a more important factor
1065 governing the seismic risk of a geothermal project compared to operational parameters.

1066 **6.1.3. Engineering parameters**

1067 **Well placement**

1068 What would be a safe distance of a geothermal well to a critically stressed fault is depending
1069 on the local geological conditions, which dictate how far pressure and stress perturbations from
1070 subsurface operations reach. Wilson et al. (2018) suggest a safe distance of fracking operations
1071 from critically stressed faults to be ~1 km. Large volume waste water injection examples
1072 suggest that faults may be triggered tens of kilometres away from injection (Goebel et al.,
1073 2017b).

1074 In balanced geothermal operations where the same amount of fluid is produced as injected a
1075 new pressure equilibrium will develop early on during operation and pore pressure increase is
1076 very limited in distances of ~1 km away from a fault. The influence of temperature induced
1077 stress changes depends on the amount of injected fluid and injection time. Typically, once the
1078 cold-water front reaches the production well, geothermal operations are stopped. Therefore, we
1079 suggest as a rule of thumb to keep the distance between geothermal wells and critically stressed
1080 faults at least to the distance between injector and producer in a geothermal doublet.
1081 Additionally, injection and production wells may be placed to limit pressure and stress
1082 perturbations to the surrounding volume (e.g., Dempsey et al., 2014; Frash et al., 2020).
1083 Furthermore, a general trend is observed that the seismic risk increases with increasing depth
1084 of injection (e.g., Hincks et al., 2018).

1085 **Net injection volume**

1086 Despite the highly complex processes underlying injection-induced seismicity, several attempts
1087 have been made to relate the maximum seismic moment to the injected volume. McGarr (2014)
1088 proposes the maximum seismic moment as the product of the injected volume (ΔV) and the
1089 shear modulus (G) of reservoir rock. However, this model may underestimate the maximum
1090 seismic moment for the case with fault rupture beyond the stimulated reservoir. A statistical
1091 model given by van der Elst et al. (2016) uses a seismogenic index (Σ) as the link between the
1092 maximum seismic moment and injected volume. Galis et al. (2017) distinguish between self-
1093 arrested and runaway ruptures, and predict the maximum seismic moment for self-arrested
1094 rupture according to the reservoir parameter (γ) and injected volume. The models introduced
1095 by van der Elst (2016) and Galis et al. (2017) are compatible with the observed data from the
1096 induced earthquakes, but the prediction accuracy is heavily dependent on the input parameters
1097 (Eaton and Igonin 2018). The models introduced by van der Elst et al. (2016) and Galis et al.
1098 (2017) are equivalent when $b=1$ and where b is the Gutenberg-Richter exponent.

1099 Figure 5 shows the maximum seismic moment as a function of injected volume. The models
1100 proposed by McGarr (2016), van der Elst et al. (2016) and Galis et al. (2017) are plotted with
1101 the data collected from various scales (Buijze et al. 2015; Galis et al. 2014; McGarr 2014). A
1102 shear modulus of 30 GPa is used to plot the model given by McGarr (2014). Three plausible
1103 reservoir parameters, e.g., 1.5×10^6 , 1.5×10^8 and 1.5×10^{10} , are considered in the model by Galis
1104 et al. (2017). The three seismogenic indices in the model by van der Elst et al. (2016)
1105 corresponding to the three plausible parameters are -1.95, -0.6 and 0.7, respectively. Despite
1106 the large scatter of the data, the maximum seismic moment roughly increases with larger
1107 injected volume, which is generally consistent with the trends predicted by the three models. In
1108 the lab scale, similar injected volume can result in far larger seismic moment by hydraulic
1109 shearing than by hydraulic fracturing, suggesting that hydraulic shearing is the major source of
1110 large seismic events. At mine and field scale, there is no clear difference anymore between
1111 maximum magnitudes induced by stimulation treatments that target hydraulic fracturing or

1112 hydroshearing. This is because seismic slip of faults, the process responsible for large seismic
1113 events, may be triggered by both applications. The maximum seismic moment for the cases
1114 with large injected volumes follows the models more closely than that for the cases with low
1115 injected volumes. This is primarily attributed to the common assumption of these models that
1116 the injection-induced moment release is purely seismic, which may be aseismic especially in
1117 the cases with low injected volumes (McGarr and Barbour 2018; De Barros et al. 2018; De
1118 Barros et al. 2019). Figure 5 also demonstrates that the model proposed by McGarr (2014)
1119 largely overestimate the maximum seismic moment for the cases with low injected volumes
1120 and underestimate some cases with large injected volumes. The models given by van der Elst
1121 et al. (2016) and Galis et al. (2017) are more consistent with the field data, showing that scaling
1122 with $\Delta V^{3/2}$ may be more suitable to predict the maximum seismic moment. Additionally, most
1123 of the cases show that the maximum seismic moment is smaller than the predicted values by
1124 the three models, indicating that the self-arrested rupture mostly occurs within the stimulated
1125 volume (Galis et al. 2017). The 2017 Pohang earthquake with moment magnitude of 5.5 largely
1126 exceeded the predicted values by the three model, because the hydraulic stimulation reactivated
1127 a previously undetected fault outside the geothermal reservoir (Lee et al. 2019). This case
1128 reveals that the maximum seismic moment is constrained not only by the injected volume but
1129 also by the tectonic stress, which is beyond the assumptions of the three models. While
1130 magnitude-net volume relations may be applied to monitor seismic risks (e.g., Hofmann et al.,
1131 2018a), the empirical evidence for the effect of volume on magnitude remains inconclusive.

1132 **Injection design**

1133 Almakari et al. (2019) find in their continuous rate- and state-dependent 2D model of a
1134 heterogeneous fault coupled with an injection-diffusion model that the total number of seismic
1135 events is controlled by the maximum pressure while the total seismic moment release increases
1136 with both maximum pressure and pressurization rate. Additionally, an increase in injection rate

1137 makes large-magnitude events more frequent. Alghannam and Juanes (2020) show with their
1138 poroelastic model of earthquake nucleation based on rate-and-state friction that the likelihood
1139 of triggering earthquakes depends rather on the pressurization rate than on the maximum
1140 pressure, suggesting that an abrupt high-rate injection protocol is likely to increase the seismic
1141 risk while a stepwise injection rate increase likely decreases seismic risk, for the same injected
1142 volume. Additionally, laboratory experiments support the hypothesis that slower pressurization
1143 rates may reduce potential injection-induced seismic hazards (Wang et al., 2020). At field scale
1144 geothermal projects, Buijze et al. (2020) find no strong correlation between increasing
1145 maximum seismic moment magnitude with injection pressure. Besides slow pressurization rates
1146 Hofmann et al. (2018a) also suggest using slow de-pressurization rates and flowback the well
1147 after stimulation operations instead of shut-in.

1148 Cyclic injection at different temporal scales was suggested to mitigate seismic risk by Hofmann
1149 et al. (2018a), Zang et al. (2019) and others. Cyclic injection procedures were applied in the
1150 context of Enhanced Geothermal System stimulation in the past years in Pohang (Hofmann et
1151 al., 2019), Helsinki (Kwiatek et al., 2019) and Reykjavik (Broccardo et al., 2020). In all cases
1152 the short-term seismic hazard was below the maximum thresholds defined for the respective
1153 projects. While the effects of cyclic injection on hydraulic fracture development were studied
1154 at multiple scales (Hofmann et al., 2018b) and fault activation has been studied under different
1155 conditions in the laboratory, no systematic comparison between the effect of continuous
1156 injection and cyclic injection on fault activation at multiple scales is yet possible.

1157 In summary, low pressurization rates, low injection pressures/rates and advanced injection
1158 protocols have the potential to reduce injection induced seismic risks in geothermal reservoirs.

1159 **Injection temperature**

1160 Buijze et al. (2020) find a weak correlation between the maximum magnitude of induced
1161 seismic events in geothermal reservoirs with increasing reservoir temperature. However, no

1162 correlation is found between temperature difference of injection water and reservoir water and
1163 the maximum moment magnitude. However, temperature changes may trigger strong thermal
1164 stresses depending on the local geological conditions as suggested by thermoelasticity theory.
1165 Thermal stresses are particularly important for geothermal reservoirs as temperature differences
1166 are typically high and long-term (decades) of cold-water injection leads to a considerable cold
1167 water plume that may induce large thermal stresses hundreds of meters away from the injection
1168 well where pressure effects typically are already very low (Figure 6).

1169 **6.2. Implications for geothermal operations**

1170 Many authors suggest methods to reduce the risk of injection-induced earthquakes (e.g.,
1171 Ellsworth, 2013; Hofmann et al., 2018; Zang et al., 2019). We divide these approaches into four
1172 major aspects: Exploration, risk assessment, monitoring, and operation.

1173 **Exploration**

1174 As shown in this review, from a geomechanics viewpoint, faults (size, orientation and
1175 properties) and stress field (directions and magnitudes or principal stresses) govern the seismic
1176 risk. Therefore, a first order risk mitigation method is a reliable identification of large critically
1177 stressed seismogenic faults before developing of a geothermal field. To minimize the risk one
1178 could then place the geothermal wells in a stable geological environment without nearby faults.

1179 However, fault are also a typical geothermal exploitation target due to increased heat and fluid
1180 flow in fault zones. Such systems are exploited all over the world (e.g. Soultz, United Downs)
1181 without inducing large magnitude seismic events. The question whether faults are rather a
1182 hazard or a target for geothermal operations remains subject to discussion.

1183 The major challenge remains, that not all faults can be identified with current exploration
1184 methods (especially in granitic basement rocks) and that stress field and fault properties often
1185 remain very poorly constrained.

1186 **Risk assessment**

1187 Similar to other industrial operations, also subsurface operations, such as injection, production
1188 or stimulation of a geothermal reservoir should be accompanied by a quantitative seismic risk
1189 assessment. This is not standard procedure yet. One example is the seismic risk assessment
1190 study by Broccardo et al. (2020) for the hydraulic stimulation treatment of a low temperature
1191 geothermal well in the city of Reykjavik.

1192 **Monitoring**

1193 The two most widely used monitoring tools for seismic hazard identification are seismic
1194 monitoring (magnitude, location, focal mechanism of seismic events) and hydraulic monitoring
1195 (injection and production rates, pressures and volumes). Parameters such as the Gutenberg-
1196 Richter b-value (lower b-value indicates more larger events and less smaller events), the
1197 relationship between injected net volume and maximum seismic moment magnitude or injected
1198 energy vs. radiated seismic energy and deviations from stable trends as well as seismic event
1199 alignment on large structures may be used for monitoring the seismic risk.

1200 Pre-defined critical observation thresholds, such as a certain peak ground velocity or magnitude
1201 of a seismic event, are used in traffic light systems to adapt operations based on such
1202 observations in order to reduce the seismic risk. However, multiple examples showed that larger
1203 magnitude events may occur even after shut-in of a geothermal well (e.g., Basel). Therefore,
1204 the concept of adaptive traffic light systems has been developed that predict future seismicity
1205 based on the hydraulic and seismic observations assuming different models and given the
1206 planned operational schedule for the site. This way, operations can be adapted early on in order
1207 to prevent large magnitude seismic events from occurring. Given the possibility of blind large
1208 scale critically stressed faults it is important to identify critical situations early on through
1209 monitoring. This is, because even small-scale pressure or stress perturbations may already
1210 trigger large magnitude seismic events.

1211 **Operation**

1212 Operational parameters that can be adjusted to alter the seismic risk may be the injection or
1213 production pressure, flow rate and volume as well as the injection temperature, the injection
1214 fluid type and the injection or production scheme. Due to the apparent importance of geological
1215 boundary conditions, no systematic relation could yet be found between largest magnitude
1216 seismic event and operational parameters in geothermal operations. Nevertheless, as a general
1217 rule, minimizing perturbations will also minimize the seismic risk. This includes maximum
1218 pressures, flow rates and pressurization rates. Another example is the multi-stage stimulation
1219 design that intends to minimize perturbations compared to massive open hole stimulations while
1220 developing a similar size total stimulated reservoir volume for production. Additionally,
1221 advanced approaches such as thermal preconditioning (Fryer et al., 2020), fracture caging
1222 (Frash et al. 20) or cyclic/adaptive injection designs (Hofmann et al., 2018a) intend to have a
1223 better control on geothermal operations. These concepts remain to be demonstrated in a
1224 sufficient number of field scale applications in order to draw firm conclusions on their potential
1225 impact.

1226

1227 **7. Conclusions**

1228 This review of models, laboratory, mine, and field scale experiments summarizes the state-of-
1229 the-art in current understanding of induced seismicity in geothermal reservoirs including
1230 hydrothermal systems and Enhanced Geothermal Systems.

1231 It is evident, that thermoelastic stress changes play an important role in induced seismic hazard
1232 in geothermal reservoirs. However, even though the theoretical framework is well established,
1233 experiments that investigate thermal effects of cold-water injection on fault slip and induced
1234 seismicity are rare and thermal effects are usually not explicitly considered in re-injection or
1235 stimulation operations.

1236

1237 **References**

1238 Alghannam, M., Juanes, R. Understanding rate effects in injection-induced earthquakes. *Nat*
1239 *Commun* 11, 3053 (2020). <https://doi.org/10.1038/s41467-020-16860-y>

1240 Almakari, M., Dublanchet, P., Chauris, H., & Pellet, F. (2019). Effect of the injection scenario
1241 on the rate and magnitude content of injection-induced seismicity: Case of a heterogeneous
1242 fault. *Journal of Geophysical Research: Solid Earth* 124:8426–8448.
1243 <https://doi.org/10.1029/2019JB017898>

1244 C. E. Bachmann, S. Wiemer, J. Woessner, S. Hainzl, Statistical analysis of the induced Basel
1245 2006 earthquake sequence: introducing a probability-based monitoring approach for Enhanced
1246 Geothermal Systems, *Geophysical Journal International*, Volume 186, Issue 2, August 2011,
1247 Pages 793–807, <https://doi.org/10.1111/j.1365-246X.2011.05068.x>

1248 Bentz, S., Kwiatek, G., Martínez-Garzón, P., Bohnhoff, M. & Dresen, G. Seismic moment
1249 evolution during hydraulic stimulations. *Geophys. Res. Lett.* 47, e2019GL086185, DOI:
1250 10.1029/2019GL086185 (2020).

1251 Bhattacharya, P., & Viesca, R. C. (2019). Fluid-induced aseismic fault slip outpaces pore-fluid
1252 migration. *Science*, 364(6439), 464-468. doi:10.1126/science.aaw7354

1253 Brace, W., & Byerlee, J. (1966). Stick-slip as a mechanism for earthquakes. *Science*, 153(3739),
1254 990-992.

1255 Blöcher, G., Cacace, M., Jacquy, A.B., Zang, A., Heidbach, O., Hofmann, H., Kluge, C., and
1256 Zimmermann, G. (2018): Evaluating Micro-Seismic Events Triggered by Reservoir Operations
1257 at the Geothermal Site of Groß Schönebeck (Germany). *Rock Mechanics and Rock Engineering*
1258 51:3265-3279.

1259 Broccardo, M., Mignan, A., Grigoli, F., Karvounis, D., Rinaldi, A. P., Danciu, L., Hofmann,
1260 H., Milkereit, C., Dahm, T., Zimmermann, G., Hjörleifsdóttir, V., and Wiemer, S. (2020):

- 1261 Induced seismicity risk analysis of the hydraulic stimulation of a geothermal well on
1262 Geldinganes, Iceland, *Nat. Hazards Earth Syst. Sci.*, 20, 1573–1593,
1263 <https://doi.org/10.5194/nhess-20-1573-2020>, 2020
- 1264 Budach, I., Moeck, I., Lüschen, E. et al. (2018). Temporal evolution of fault systems in the
1265 Upper Jurassic of the Central German Molasse Basin: case study Unterhaching. *Int J Earth Sci*
1266 (*Geol Rundsch*) 107, 635–653. <https://doi.org/10.1007/s00531-017-1518-1>
- 1267 Buijze, L., Wassing, B., Fokker, P., & Van Wees, J. (2015). Moment Partitioning for Injection-
1268 Induced Seismicity: Case Studies & Insights from Numerical Modeling. Paper presented at the
1269 World Geothermal Congress.
- 1270 Byerlee J (1978) Friction of rocks. *Pure Appl Geophys PAGEOPH* 116(4–5):615–626.
1271 <https://doi.org/10.1007/BF00876528>
- 1272 Cacace M, Jacquy AB (2017) Flexible parallel implicit modelling of coupled thermal–
1273 hydraulic–mechanical processes in fractured rocks. *Solid Earth* 8(5):921-941
- 1274 Cappa, F., Guglielmi, Y., Nussbaum, C., & Birkholzer, J. (2018). On the relationship between
1275 fault permeability increases, induced stress perturbation and the growth of aseismic slip during
1276 fluid injection. *Geophysical Research Letters*, 45(20), 11,012-011,020.
1277 [doi:10.1029/2018gl080233](https://doi.org/10.1029/2018gl080233)
- 1278 Cappa, F., Scuderi, M. M., Collettini, C., Guglielmi, Y., & Avouac, J.-P. (2019). Stabilization
1279 of fault slip by fluid injection in the laboratory and in situ. *Science advances*, 5(3), eaau4065.
1280 [doi:10.1126/sciadv.aau4065](https://doi.org/10.1126/sciadv.aau4065)
- 1281 Catalli, F., Meier, M.-A., Wiemer, S. (2013): The role of Coulomb stress changes for injection-
1282 induced seismicity: The Basel enhanced geothermal system. *Geophysical Research Letters*
1283 40(1):72-77. <https://doi.org/10.1029/2012GL054147>

- 1284 Cebry, S. B. L., & McLaskey, G. C. (2021). Seismic swarms produced by rapid fluid injection
1285 into a low permeability laboratory fault. *Earth and Planetary Science Letters*, 557, 116726.
1286 doi:<https://doi.org/10.1016/j.epsl.2020.116726>
- 1287 Cochran, E.S., Vidale, J.E., & Tanaka, S. (2004). Earth tides can trigger shallow thrust fault
1288 earthquakes. *Science*, 306, 1164-1166.
- 1289 Cornelio, C., & Violay, M. (2020). Effect of Fluid Viscosity on Earthquake Nucleation.
1290 *Geophysical Research Letters*, 47(12). doi:10.1029/2020gl087854
- 1291 Cornelio, C., Passelègue, F. X., Spagnuolo, E., Di Toro, G., & Violay, M. (2020). Effect of
1292 Fluid Viscosity on Fault Reactivation and Coseismic Weakening. *Journal of Geophysical*
1293 *Research: Solid Earth*, 125(1). doi:10.1029/2019jb018883
- 1294 Cornelio, C., Spagnuolo, E., Di Toro, G., Nielsen, S., & Violay, M. (2019). Mechanical
1295 behaviour of fluid-lubricated faults. *Nature Communications*, 10(1), 1-7. doi:10.1038/s41467-
1296 019-09293-9
- 1297 De Barros, L., Cappa, F., Guglielmi, Y., Duboeuf, L., & Grasso, J. R. (2019). Energy of
1298 injection-induced seismicity predicted from in-situ experiments. *Scientific Reports*, 9(1), 4999.
1299 doi:10.1038/s41598-019-41306-x
- 1300 De Barros, L., Guglielmi, Y., Rivet, D., Cappa, F., & Duboeuf, L. (2018). Seismicity and fault
1301 aseismic deformation caused by fluid injection in decametric in-situ experiments. *Comptes*
1302 *Rendus Geoscience*, 350(8), 464-475. doi:10.1016/j.crte.2018.08.002
- 1303 De Barros, L., Daniel, G., Guglielmi, Y., Rivet, D., Caron, H., Payre, X., . . . Gourlay, M.
1304 (2016). Fault structure, stress, or pressure control of the seismicity in shale? Insights from a
1305 controlled experiment of fluid-induced fault reactivation. *Journal of Geophysical Research:*
1306 *Solid Earth*, 121(6), 4506-4522. doi:10.1002/2015JB012633

- 1307 Deichmann N, Kraft T, Evans KF (2014) Identification of faults activated during the stimulation
1308 of the Basel geothermal project from cluster analysis and focal mechanisms of the larger
1309 magnitude events. *Geothermics* 52:84-97. <https://doi.org/10.1016/j.geothermics.2014.04.001>
- 1310 David Dempsey, Sharad Kelkar, Rajesh Pawar, Passive injection: A strategy for mitigating
1311 reservoir pressurization, induced seismicity and brine migration in geologic CO₂ storage,
1312 *International Journal of Greenhouse Gas Control*, Volume 28, 2014, Pages 96-113,
1313 <https://doi.org/10.1016/j.ijggc.2014.06.002>.
- 1314 Derode, B., Guglielmi, Y., De Barros, L., & Cappa, F. (2015). Seismic responses to fluid
1315 pressure perturbations in a slipping fault. *Geophysical Research Letters*, 42(9), 3197-3203.
1316 doi:10.1002/2015gl063671
- 1317 James H. Dieterich, Keith B. Richards-Dinger, Kayla A. Kroll (2015). Modeling Injection-
1318 Induced Seismicity with the Physics-Based Earthquake Simulator RSQSim. *Seismological*
1319 *Research Letters* 86(4):1102–1109. doi: <https://doi.org/10.1785/0220150057>
- 1320 Dresen, G., Kwiatek, G., Goebel, T., & Ben-Zion, Y. (2020). Seismic and Aseismic Preparatory
1321 Processes Before Large Stick–Slip Failure. *Pure and Applied Geophysics*, 1-20.
1322 doi:10.1007/s00024-020-02605-x
- 1323 Duboeuf, L., De Barros, L., Cappa, F., Guglielmi, Y., Deschamps, A., & Seguy, S. (2017).
1324 Aseismic motions drive a sparse seismicity during fluid injections into a fractured zone in a
1325 carbonate reservoir. *Journal of Geophysical Research: Solid Earth*, 122(10), 8285-8304.
1326 doi:10.1002/2017jb014535
- 1327 Eaton, D. W., & Igonin, N. (2018). What controls the maximum magnitude of injection-induced
1328 earthquakes? *The Leading Edge*, 37(2), 135-140.
- 1329 Ellsworth, W.L. (2013): Injection-Induced Earthquakes. *Science* 341(6142):1225942.
1330 <https://doi.org/10.1126/science.1225942>

- 1331 Fang, Y., Elsworth, D., Ishibashi, T., & Zhang, F. (2018). Permeability Evolution and Frictional
1332 Stability of Fabricated Fractures With Specified Roughness. *Journal of Geophysical Research:*
1333 *Solid Earth*, 123, 9355–9375. doi:10.1029/2018jb016215
- 1334 Fang, Y., Elsworth, D., Wang, C., Ishibashi, T., & Fitts, J. P. (2017). Frictional stability-
1335 permeability relationships for fractures in shales. *Journal of Geophysical Research: Solid Earth*,
1336 122(3), 1760–1776. doi:10.1002/2016jb013435
- 1337 Foulger, G.R., Wilson, M., Gluyas, J., Julian, B.R., Davies, R. (2018). Global review of human-
1338 induced earthquakes. *Earth-Science Reviews*, 178, 438-514.
1339 <https://doi.org/10.1016/j.earscirev.2017.07.008>
- 1340 Frash, L.P., Fu, P., Morris, J., Gutierrez, M., Neupane, G., Hampton, J., Welch, N.J., Carey,
1341 J.W., Kneafsey, T. (2021): Fracture caging to limit induced seismicity. *Geophysical Research*
1342 *Letters* 48(1):e2020GL090648. <https://doi.org/10.1029/2020GL090648>
- 1343 B Fryer, G Siddiqi, L Laloui, Injection-induced seismicity: strategies for reducing risk using
1344 high stress path reservoirs and temperature-induced stress preconditioning, *Geophysical*
1345 *Journal International*, Volume 220, Issue 2, February 2020, Pages 1436–1446,
1346 <https://doi.org/10.1093/gji/ggz490>
- 1347 Galis, M., Ampuero, J. P., Mai, P. M., & Cappa, F. (2017). Induced seismicity provides insight
1348 into why earthquake ruptures stop. *Science advances*, 3(12), eaap7528.
1349 doi:10.1126/sciadv.aap7528
- 1350 Gischig, V. S., Giardini, D., Amann, F., Hertrich, M., Krietsch, H., Loew, S., . . . Valley, B.
1351 (2019). Hydraulic stimulation and fluid circulation experiments in underground laboratories:
1352 Stepping up the scale towards engineered geothermal systems. *Geomechanics for Energy and*
1353 *the Environment*. doi:10.1016/j.gete.2019.100175

1354 Goebel, T. H. W., Kwiatek, G., Becker, T. W., Brodsky, E. E., & Dresen, G. (2017a). What
1355 allows seismic events to grow big?: Insights from b-value and fault roughness analysis in
1356 laboratory stick-slip experiments. *Geology*, 45(9), 815-818. doi:10.1130/g39147.1

1357 T.H.W. Goebel, M. Weingarten, X. Chen, J. Haffener, E.E. Brodsky (2017b). The 2016 Mw5.1
1358 Fairview, Oklahoma earthquakes: Evidence for long-range poroelastic triggering at >40 km
1359 from fluid disposal wells. *Earth and Planetary Science Letters* 472:50-61,
1360 <https://doi.org/10.1016/j.epsl.2017.05.011>

1361 Goodfellow, S. D., Nasser, M. H. B., Maxwell, S. C., & Young, R. P. (2015). Hydraulic
1362 fracture energy budget: Insights from the laboratory. *Geophysical Research Letters*, 42(9),
1363 3179-3187. doi:10.1002/2015gl063093

1364 S. Gudbrandsson, D. Wolff-Boenisch, S. R. Gislason, and E. H. Oelkers, “Experimental
1365 determination of plagioclase dissolution rates as a function of its composition and pH at 22 °C,”
1366 *Geochimica et Cosmochimica Acta*, vol. 139, pp. 154–172, 2014.

1367 Guglielmi, Y., Cappa, F., Avouac, J.-P., Henry, P., & Elsworth, D. (2015a). Seismicity
1368 triggered by fluid injection–induced aseismic slip. *Science*, 348(6240), 1224-1226.
1369 doi:10.1126/science.aab0476

1370 Guglielmi, Y., Cappa, F., Avouac, J.-P., Henry, P., & Elsworth, D. (2015b). Seismicity
1371 triggered by fluid injection–induced aseismic slip. *Science*, 348(6240), 1224-1226.
1372 doi:10.1126/science.aab0476

1373 Guglielmi, Y., Nussbaum, C., Jeanne, P., Rutqvist, J., Cappa, F., & Birkholzer, J. (2020).
1374 Complexity of Fault Rupture and Fluid Leakage in Shale: Insights from a Controlled Fault
1375 Activation Experiment. *Journal of Geophysical Research: Solid Earth*, 125(2), e2019JB017781.
1376 doi:10.1029/2019jb017781

1377 Harris, R., Simpson, R. Changes in static stress on southern California faults after the 1992
1378 Landers earthquake. *Nature* 360, 251–254 (1992). <https://doi.org/10.1038/360251a0>

1379 Hassanzadegan, A., Blöcher, G., Zimmermann, G., Milsch, H., Moeck, I. (2011). Induced
1380 Stress in a Geothermal Doublet System, PROCEEDINGS, Thirty-Sixth Workshop on
1381 Geothermal Reservoir Engineering Stanford University, Stanford, California, January 31 -
1382 February 2, 2011 SGP-TR-191.

1383 Hassanzadegan A, Blöcher G, Zimmermann G, Milsch H (2012). Thermoporoelastic properties
1384 of Flechtinger sandstone. *Int J Rock Mech Min* 49(0):94–104

1385 Hincks, T., Aspinall, W., Cooke, R., Gernon, T. (2018): Oklahoma's induced seismicity
1386 strongly linked to wastewater injection depth. *Science* 359(6381):1251-1255.
1387 <https://doi.org/10.1126/science.aap7911>

1388 Hofmann, H., Zimmermann, G., Farkas, M., Huenges, E., Zang, A., Leonhardt, M., . . . Kim,
1389 K. Y. (2019). First field application of cyclic soft stimulation at the Pohang Enhanced
1390 Geothermal System site in Korea. *Geophysical Journal International*, 217(2), 926-949.
1391 doi:10.1093/gji/ggz058

1392 Hofmann, H., Zimmermann, G., Zang, A., & Min, K.-B. (2018a). Cyclic soft stimulation (CSS):
1393 a new fluid injection protocol and traffic light system to mitigate seismic risks of hydraulic
1394 stimulation treatments. *Geothermal Energy*, 6(1), 27.

1395 Hofmann, H., Zimmermann, G., Zang, A., Yoon, J.S., Stephansson, O., Kim, K.Y., Zhuang, L.,
1396 Diaz, M., Min, K.-B. (2018b): Comparison of cyclic and constant fluid injection in granitic rock
1397 at different scales. 52nd US Rock Mechanics / Geomechanics Symposium, Seattle,
1398 Washington, USA, 17-20 June 2018. ARMA 18-691.

- 1399 Hummel, N., & Shapiro, S. A. (2013). Nonlinear diffusion-based interpretation of induced
1400 microseismicity: A Barnett Shale hydraulic fracturing case study. *Geophysics*, 78(5), B211-
1401 B226. <https://doi.org/10.1190/geo2012-0242.1>
- 1402 Ishibashi, T., Elsworth, D., Fang, Y., Riviere, J., Madara, B., Asanuma, H., . . . Marone, C.
1403 (2018). Friction-stability-permeability evolution of a fracture in granite. *Water Resources*
1404 *Research*, 54, 9901–9918. doi:10.1029/2018WR022598
- 1405 Jeanne, P., Guglielmi, Y., Rutqvist, J., Nussbaum, C., & Birkholzer, J. (2018). Permeability
1406 Variations Associated With Fault Reactivation in a Claystone Formation Investigated by Field
1407 Experiments and Numerical Simulations. *Journal of Geophysical Research: Solid Earth*, 123(2),
1408 1694-1710. doi:10.1002/2017jb015149
- 1409 Jeanne, P., Guglielmi, Y., Rutqvist, J., Nussbaum, C., & Birkholzer, J. (2017). Field
1410 characterization of elastic properties across a fault zone reactivated by fluid injection. *Journal*
1411 *of Geophysical Research: Solid Earth*, 122(8), 6583-6598.
- 1412 Ji, Y., & Wu, W. (2020). Injection-driven fracture instability in granite: Mechanism and
1413 implications. *Tectonophysics*, 791, 228572. doi:10.1016/j.tecto.2020.228572
- 1414 Ji, Y., Wanniarachchi, W. A. M., & Wu, W. (2020). Effect of fluid pressure heterogeneity on
1415 injection-induced fracture activation. *Computers and Geotechnics*, 123, 103589.
1416 doi:10.1016/j.compgeo.2020.103589
- 1417 Ji Y, Yoon JS, Zang A, Wu W (2021a) Shear stress transfer induced by fluid overpressurization
1418 and implications for injectioninduced fault activation in crystalline rocks. *Earth Planet Sci Lett*,
1419 (Under review)
- 1420 Ji, Y., Yoon, J. S., Zang, A., & Wu, W. (2021b). Mitigation of injection-induced seismicity on
1421 undrained faults in granite using cyclic fluid injection. *International Journal of Rock Mechanics*
1422 *and Mining Sciences*, (Under review)

- 1423 Ji, Y., Zhuang, L., Wu, W., Hofmann, H., Zang, A., & Zimmermann, G. (2021c). Cyclic water
1424 injection potentially mitigates seismic risks by promoting slow and stable slip of a natural
1425 fracture in granite. *Rock Mechanics and Rock Engineering*, (Under review)
- 1426 Ji, Y., Hofmann, H., Duan, K., Zang, A. (2022). Laboratory experiments on fault behaviour
1427 towards better understanding of injection-induced seismicity in geoenery systems. *Earth-*
1428 *Science Reviews* 226, 103916. <https://doi.org/10.1016/j.earscirev.2021.103916>
- 1429 Johann, L., Shapiro, S.A., and Dinske, C. (2018). The surge of earthquakes in Central Oklahoma
1430 has features of reservoir-induced seismicity. *Scientific reports* 8, 11505.
1431 <https://doi.org/10.1038/s41598-018-29883-9>
- 1432 Johann, L., Dinske, C., & Shapiro, S. A. (2016). Scaling of seismicity induced by nonlinear
1433 fluid-rock interaction after an injection stop. *Journal of Geophysical Research: Solid Earth*,
1434 121(11), 8154-8174. <https://doi.org/10.1002/2016JB012949>
- 1435 Kakurina, M., Guglielmi, Y., Nussbaum, C., & Valley, B. (2019). Slip perturbation during fault
1436 reactivation by a fluid injection. *Tectonophysics*, 757, 140-152.
1437 doi:10.1016/j.tecto.2019.01.017
- 1438 Kohli, A. H., & Zoback, M. D. (2013). Frictional properties of shale reservoir rocks. *Journal of*
1439 *Geophysical Research: Solid Earth*, 118(9), 5109-5125. doi:10.1002/jgrb.50346
- 1440 Kolawole F, Johnston CS, Morgan CB, Chang JC, Marfurt KJ, Lockner DA, Reches Z,
1441 Carpenter BM (2019) The susceptibility of Oklahoma's basement to seismic reactivation.
1442 *Nature Geoscience* 12(10):839-844
- 1443 Kroll, K.A., Richards-Dinger, K.B., Dieterich, J.H. (2017): Sensitivity of induced seismic
1444 sequences to rate-and-state frictional processes. *Journal of Geophysical Research Solid Earth*
1445 122(12):10207-10219. <https://doi.org/10.1002/2017JB014841>

- 1446 Kwiatek, G., Saarno, T., Ader, T., Bluemle, F., Bohnhoff, M., et al. (2019): Controlling fluid-
1447 induced seismicity during a 6.1-km-deep geothermal stimulation in Finland. *Science Advances*
1448 5(5):eaav7224. <https://doi.org/10.1126/sciadv.aav7224>
- 1449 Kwiatek, G., Bohnhoff, M., Dresen, G., Schulze, A., Schulte, T., Zimmermann, G., Huenges, E.
1450 (2010): Microseismicity Induced During Fluid-Injection: A Case Study from the Geothermal
1451 Site at Groß Schönebeck, North German Basin. *Acta Geophysica* 58(6):995-1020.
1452 <https://doi.org/10.2478/s11600-010-0032-7>
- 1453 Lee, K.-K., Ellsworth, W. L., Giardini, D., Townend, J., Ge, S., Shimamoto, T., . . .
1454 Langenbruch, C. (2019). Managing injection-induced seismic risks. *Science*, 364(6442), 730-
1455 732. doi:10.1126/science.aax1878
- 1456 Li X, Liang Y, Luo Y, Ai C (2020) Predicting hydraulic fracture propagation based on
1457 maximum energy release rate theory with consideration of T-stress. *Fuel* 269:117337
- 1458 Ma, J., Ahkami, M., Saar, M. O., & Kong, X.-Z. (2021). Quantification of mineral accessible
1459 surface area and flow-dependent fluid-mineral reactivity at the pore scale. *Chemical Geology*,
1460 120042. doi:<https://doi.org/10.1016/j.chemgeo.2020.120042>
- 1461 McGarr, A. (2014). Maximum magnitude earthquakes induced by fluid injection. *Journal of*
1462 *Geophysical Research: Solid Earth*, 119(2), 1008-1019. doi:10.1002/2013jb010597
- 1463 McGarr, A., & Barbour, A. J. (2018). Injection-induced moment release can also be aseismic.
1464 *Geophysical Research Letters*, 45, 5344-5351. doi:10.1029/2018GL078422
- 1465 Noël, C., Passelègue, F. X., Giorgetti, C., & Violay, M. (2019). Fault Reactivation During Fluid
1466 Pressure Oscillations: Transition From Stable to Unstable Slip. *Journal of Geophysical*
1467 *Research: Solid Earth*, 124, 10940–10953. doi:10.1029/2019jb018517
- 1468 Parisio, F., Vilarrasa, V., Wang, W. et al. The risks of long-term re-injection in supercritical
1469 geothermal systems. *Nat Commun* 10, 4391 (2019). <https://doi.org/10.1038/s41467-019->
KEM-15 A1 Key parameters affecting induced seismicity in geothermal reservoirs across scale

- 1470 12146-0Passelegue, F. X., Brantut, N., & Mitchell, T. M. (2018). Fault reactivation by fluid
1471 injection: Controls from stress state and injection rate. *Geophysical Research Letters*, 45(23),
1472 12,837– 812,846. doi:doi:10.1029/2018GL080470
- 1473 Pei L, Blöcher G, Milsch H, Zimmermann G, Sass I, Huenges E. Thermo-mechanical properties
1474 of Upper Jurassic (Malm) carbonate rock under drained conditions. *Rock Mech Rock Eng.*
1475 2018; 51(1):23-45.
- 1476 Pei, L., Blöcher, G., Milsch, H., Zimmermann, G., Zhang, H., Lib, X., Huenges, E. (2020).
1477 Analysis of measured thermally induced rock deformation, *Measurement* 163 (2020) 108004.
- 1478 Rice JR (1993) Spatio-temporal complexity of slip on a fault. *J Geophys Res Solid Earth*
1479 98(B6):9885-9907
- 1480 Rinaldi AP, Rutqvist J (2019) Joint opening or hydroshearing? Analyzing a fracture zone
1481 stimulation at Fenton Hill. *Geothermics* 77:83-98
- 1482 Polak, A., Elsworth, D., Yasuhara, H., Grader, A. S., & Halleck, P. M. (2003). Permeability
1483 reduction of a natural fracture under net dissolution by hydrothermal fluids. *Geophysical*
1484 *Research Letters*, 30(20). doi:10.1029/2003GL017575
- 1485 Rutter, E. H., & Mecklenburgh, J. (2018). Influence of Normal and Shear Stress on the
1486 Hydraulic Transmissivity of Thin Cracks in a Tight Quartz Sandstone, a Granite, and a Shale.
1487 *Journal of Geophysical Research: Solid Earth*, 123(2), 1262-1285. doi:10.1002/2017jb014858
- 1488 Schmittbuhl, J., Lambotte, S., Lengliné, O., Grunberg, M., Jund, H., Vergne, J., Cornet, F.,
1489 Doubre, C., Masson, F. (2021). Induced and triggered seismicity below the city of Strasbourg,
1490 France from November 2019 to January 2021. *Comptes Rendus. Geoscience*, 353, S1, 561-584.
1491 <https://doi.org/10.5802/crgeos.71>
- 1492 Scholz, C. H. (1998). Earthquakes and friction laws. *Nature*, 391(6662), 37-42.
1493 doi:10.1038/34097

- 1494 Scuderi, M. M., & Collettini, C. (2018). Fluid Injection and the Mechanics of Frictional
1495 Stability of Shale-Bearing Faults. *Journal of Geophysical Research: Solid Earth*, 123(10), 8364-
1496 8384. doi:10.1029/2018jb016084
- 1497 Scuderi, M. M., Collettini, C., & Marone, C. (2017). Frictional stability and earthquake
1498 triggering during fluid pressure stimulation of an experimental fault. *Earth and Planetary
1499 Science Letters*, 477, 84-96. doi:10.1016/j.epsl.2017.08.009
- 1500 Scuderi, M. M., & Collettini, C. (2016). The role of fluid pressure in induced vs. triggered
1501 seismicity: insights from rock deformation experiments on carbonates. *Scientific Reports*, 6(1),
1502 1-9. doi:10.1038/srep24852
- 1503 Segall, P., & Fitzgerald, S. (1998). A note on induced stress changes in hydrocarbon and
1504 geothermal reservoir, *Tectonophysics*, 289, 117-128.
- 1505 Shang, D., Zhao, Z., Dou, Z., & Yang, Q. (2020). Shear behaviors of granite fractures immersed
1506 in chemical solutions. *Engineering Geology*, 279, 105869.
1507 doi:<https://doi.org/10.1016/j.enggeo.2020.105869>
- 1508 Shapiro, S. A. (2018). Seismogenic index of underground fluid injections and
1509 productions. *Journal of Geophysical Research: Solid Earth*, 123.
1510 <https://doi.org/10.1029/2018JB015850>
- 1511 Shapiro, S. A., Krüger, O. S., Dinske, C., & Langenbruch, C. (2011). Magnitudes of induced
1512 earthquakes and geometric scales of fluid-stimulated rock volumes. *Geophysics*, 76(6), WC55-
1513 WC63.
- 1514 Shapiro, S. A., & Dinske, C. (2009). Scaling of seismicity induced by nonlinear fluid-rock
1515 interaction. *Journal of Geophysical Research: Solid Earth*, 114(B9).
1516 <https://doi.org/10.1029/2008JB006145>

1517 Stein, R.S., Lisowski, M. (1983): The 1979 Homestead Valley Earthquake Sequence,
 1518 California: Control of aftershocks and postseismic deformation. *Journal of Geophysical*
 1519 *Research Solid Earth* 88(B8):6477-6490. <https://doi.org/10.1029/JB088iB08p06477>

1520 van der Elst, N. J., Page, M. T., Weiser, D. A., Goebel, T. H. W., & Hosseini, S. M. (2016).
 1521 Induced earthquake magnitudes are as large as (statistically) expected. *Journal of Geophysical*
 1522 *Research: Solid Earth*, 121(6), 4575-4590. doi:doi:10.1002/2016JB012818

1523 Wang, J., Ge, H., Wang, X., Shen, Y., Liu, T., Zhang, Y., & Meng, F. (2019). Effect of Clay
 1524 and Organic Matter Content on the Shear Slip Properties of Shale. *Journal of Geophysical*
 1525 *Research: Solid Earth*, 124(9), 9505-9525. doi:10.1029/2018jb016830

1526 Wang, L., Kwiatek, G., Rybacki, E., Bonnelye, A., Bohnhoff, M., & Dresen, G. (2020).
 1527 Laboratory study on fluid-induced fault slip behavior: The role of fluid pressurization rate.
 1528 *Geophysical Research Letters*, 47, e2019GL086627. doi:10.1029/2019gl086627

1529 Rob Westaway, Neil M. Burnside, "Fault "Corrosion" by Fluid Injection: A Potential Cause of
 1530 the November 2017 5.5 Korean Earthquake", *Geofluids*, vol. 2019, Article ID 1280721, 23
 1531 pages, 2019. <https://doi.org/10.1155/2019/1280721>

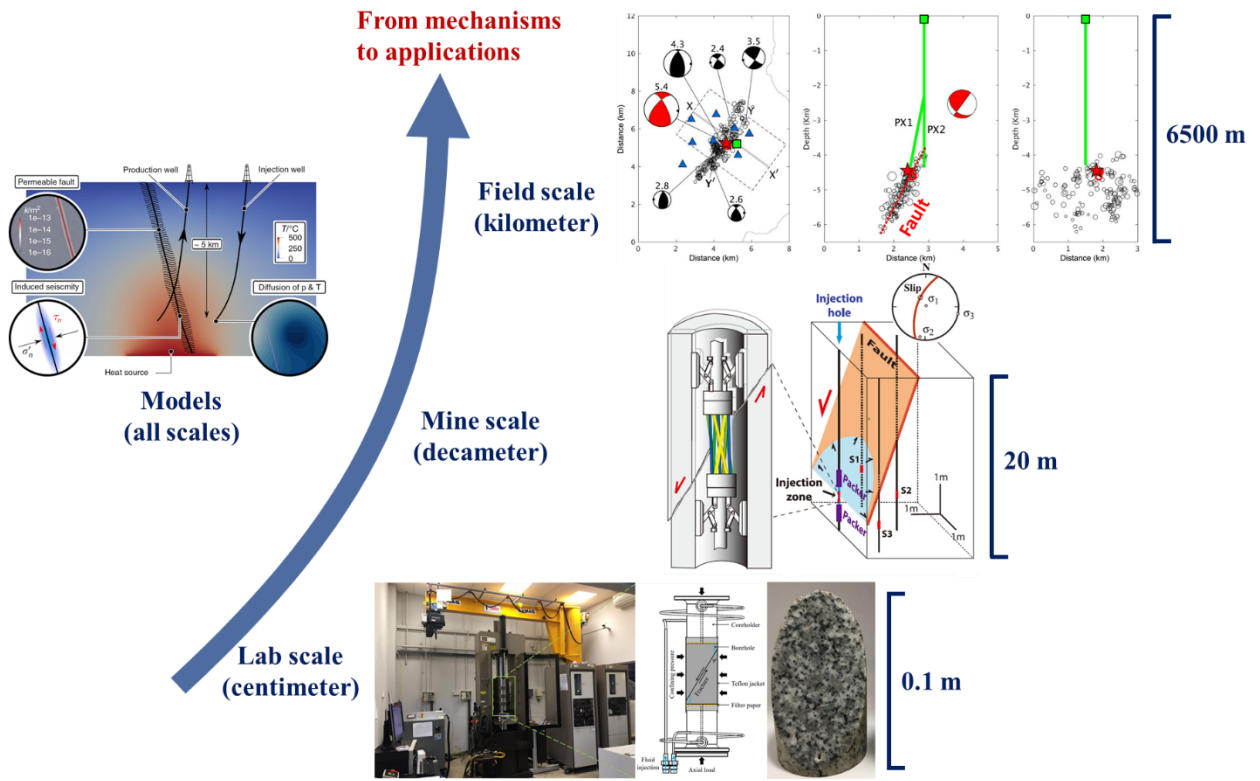
1532 Wong, T.-F., Brace, W.F. (1979). Thermal expansion of rocks: some measurements at high
 1533 pressure, *Tectonophysics*, 57, 95-117.

1534 Woo, J.-U. et al. An in-depth seismological analysis revealing a causal link between the 2017
 1535 MW 5.5 Pohang earthquake and EGS project. *J. Geophys. Res. Solid Earth* 124, 13060–13078,
 1536 DOI: 10.1029/2019JB018368 (2019).

1537 Wynants-Morel, N., Cappa, F., de Barros, L., Ampuero, J.-P. (2020): Stress Perturbation From
 1538 Aseismic Slip Drives the Seismic Front During Fluid Injection in a Permeable Fault. *Journal of*
 1539 *Geophysical Research: Solid Earth* 125(7):e2019JB019179.
 1540 <https://doi.org/10.1029/2019JB019179>

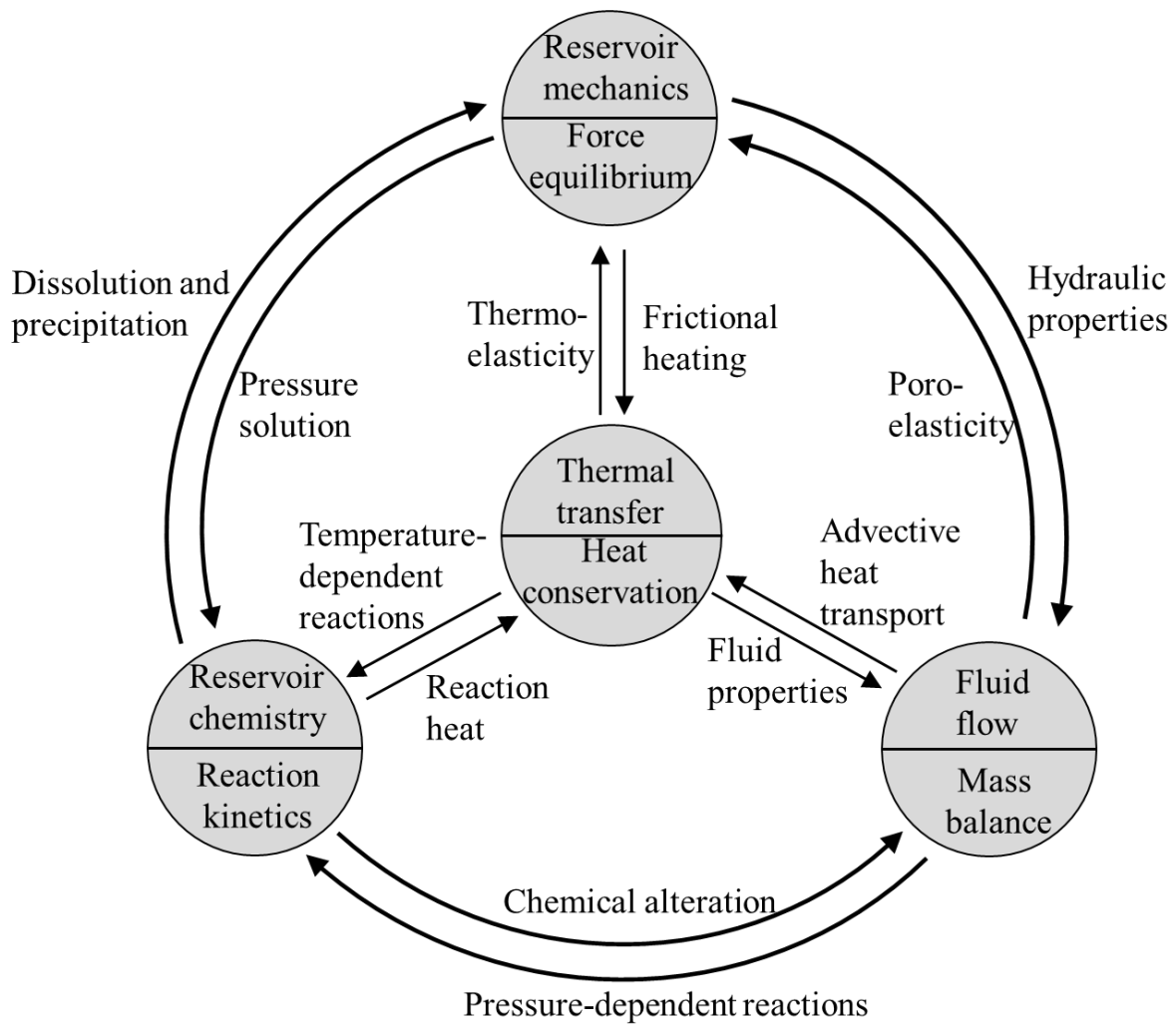
- 1541 Xing, T., Zhu, W., French, M., & Belzer, B. (2019). Stabilizing Effect of High Pore Fluid
1542 Pressure on Slip Behaviors of Gouge-bearing Faults. *Journal of Geophysical Research: Solid*
1543 *Earth*. doi:10.1029/2019jb018002
- 1544 Yarushina, V. M., & Bercovici, D. (2013). Mineral carbon sequestration and induced
1545 seismicity. *Geophysical Research Letters*, 40(5), 814-818.
1546 doi:<https://doi.org/10.1002/grl.50196>
- 1547 H. Yasuhara, C. Marone, and D. Elsworth, "Fault zone restrengthening and frictional healing:
1548 the role of pressure solution," *Journal of Geophysical Research*, vol. 110, no. B6, article
1549 B06310, 2005.
- 1550 Yasuhara, H., Elsworth, D., & Polak, A. (2004). Evolution of permeability in a natural fracture:
1551 Significant role of pressure solution. *Journal of Geophysical Research: Solid Earth*, 109(B3).
1552 doi:10.1029/2003JB002663
- 1553 Zang, A., Yoon, J. S., Stephansson, O., & Heidbach, O. (2013). Fatigue hydraulic fracturing by
1554 cyclic reservoir treatment enhances permeability and reduces induced seismicity. *Geophysical*
1555 *Journal International*, 195(2), 1282-1287.
- 1556 Zang, A., Zimmermann, G., Hofmann, H., Stephansson, O., Min, K.-B., & Kim, K. Y. (2019).
1557 How to Reduce Fluid-Injection-Induced Seismicity. *Rock Mechanics and Rock Engineering*,
1558 52(2), 475-493. doi:10.1007/s00603-018-1467-4
- 1559 Zhang W, Mehrabian A (2020) Poroelastic Solution for the Nonlinear Injectivity of Subsurface
1560 Rocks With Strain-Induced Permeability Variations. *Water Resources Research*
1561 56(8):e2020WR027620
- 1562 Zhou C, Wan Z, Zhang Y, Gu B (2018) Experimental study on hydraulic fracturing of granite
1563 under thermal shock. *Geothermics* 71:146-155

- 1564 Zhu W, Allison KL, Dunham EM, Yang Y (2020) Fault valving and pore pressure evolution in
1565 simulations of earthquake sequences and aseismic slip. *Nature Communications* 11(1):4833
- 1566 Ziegler, M.O., Heidbach, O (2020). The 3D stress state from geomechanical–numerical
1567 modelling and its uncertainties: a case study in the Bavarian Molasse Basin. *Geotherm Energy*
1568 8, 11. <https://doi.org/10.1186/s40517-020-00162-z>
- 1569 Zimmerman RW (2000) Coupling in poroelasticity and thermoelasticity. *Int J Rock Mech Min*
1570 37(1–2):79–87
- 1571 Zoback MD (2007) *Reservoir geomechanics*. Cambridge University Press, Cambridge.
1572 <https://doi.org/10.1017/CBO9780511586477>



1574

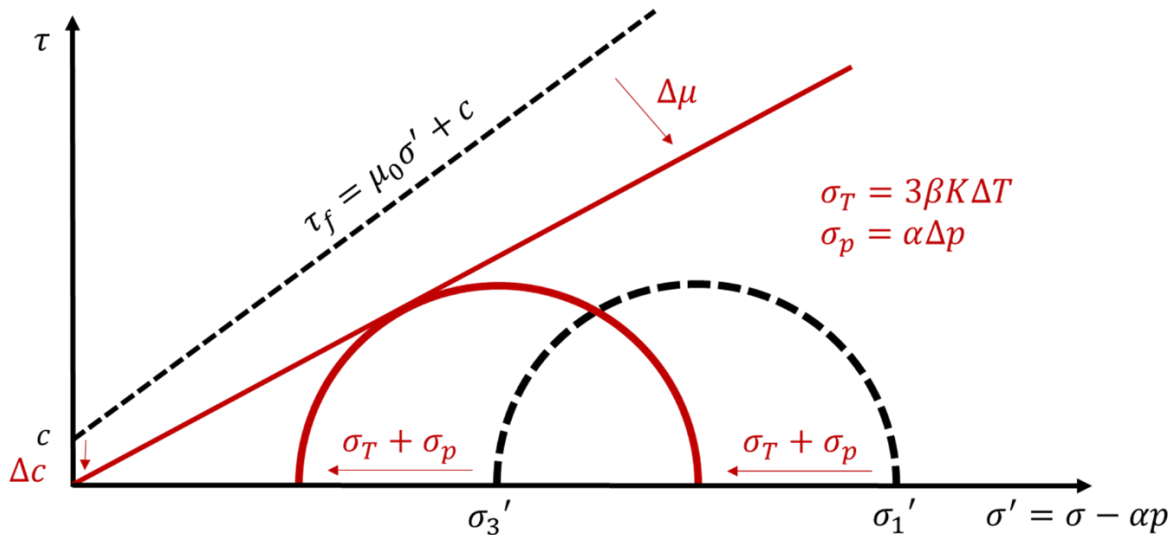
1575 *Figure 1: A multi-scale experimental and modelling approach is proposed to improve the*
 1576 *understanding of injection induced seismicity in geothermal reservoirs (Figure based on*
 1577 *Parisio et al., 2019, Kim et al, 2018, and Lee and Guglielmi, 2015a).*



1578

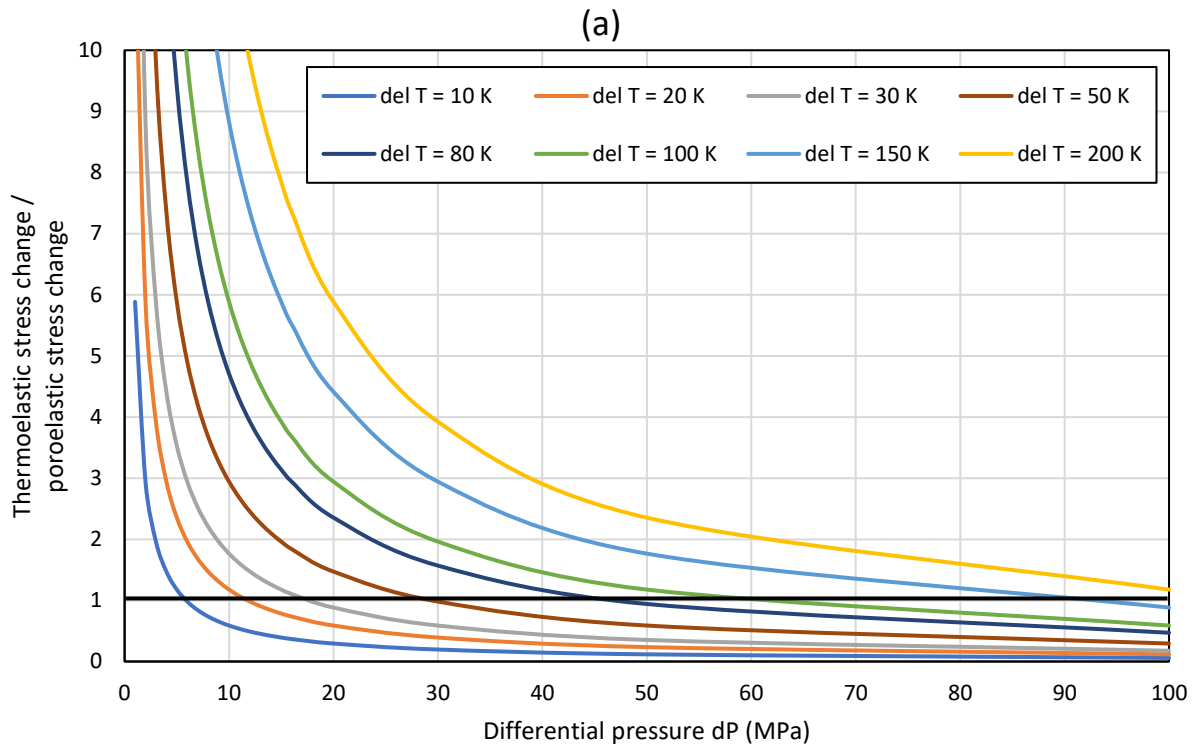
1579 *Figure 2: Schematic of coupled thermo-hydro-mechanical-chemical processes relevant for*
 1580 *induced seismicity in geothermal reservoirs (based on Gaucher et al., 2015).*

1581

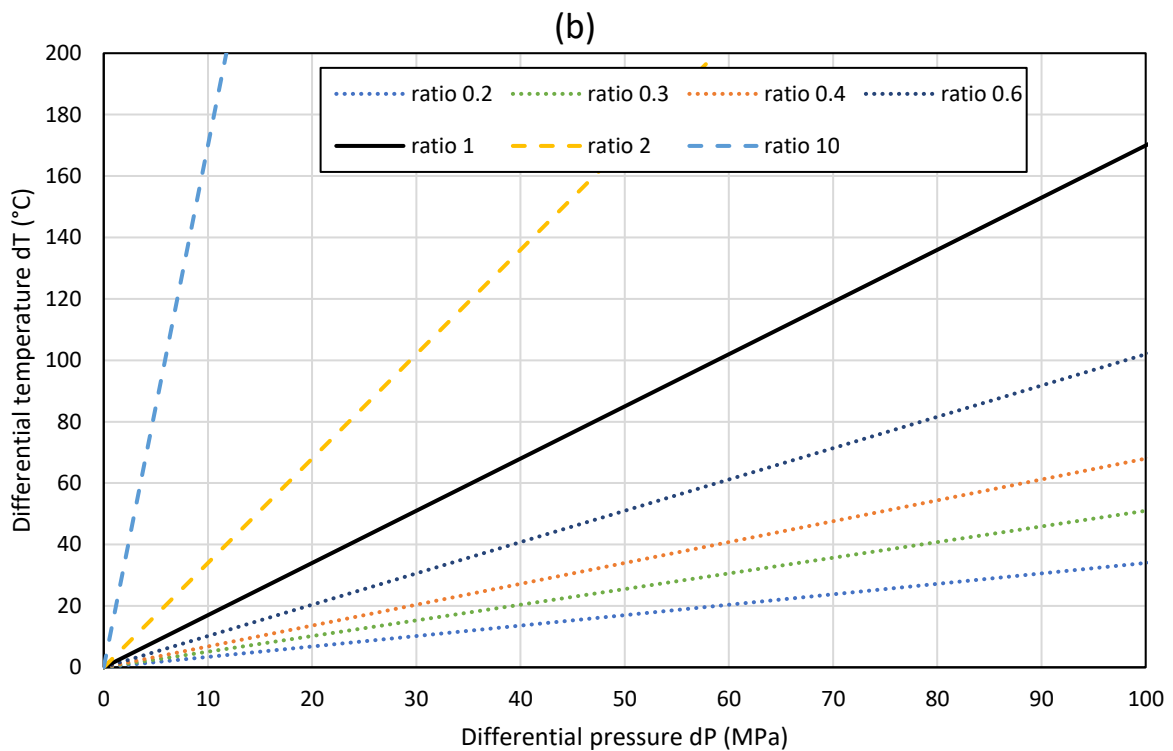


1582
 1583
 1584
 1585
 1586
 1587
 1588
 1589

Figure 3: Both, pressure increase Δp and temperature reduction ΔT lead to a reduction in effective stresses σ' , thus promoting failure, depending on the effective stress coefficient α (not the same as the Biot coefficient when considering fault stability), thermal expansion coefficient β , Bulk modulus K and the actual pressure and temperature change. Additionally, a reduction in friction coefficient μ and cohesion c , for example through mineral dissolution, may trigger failure.



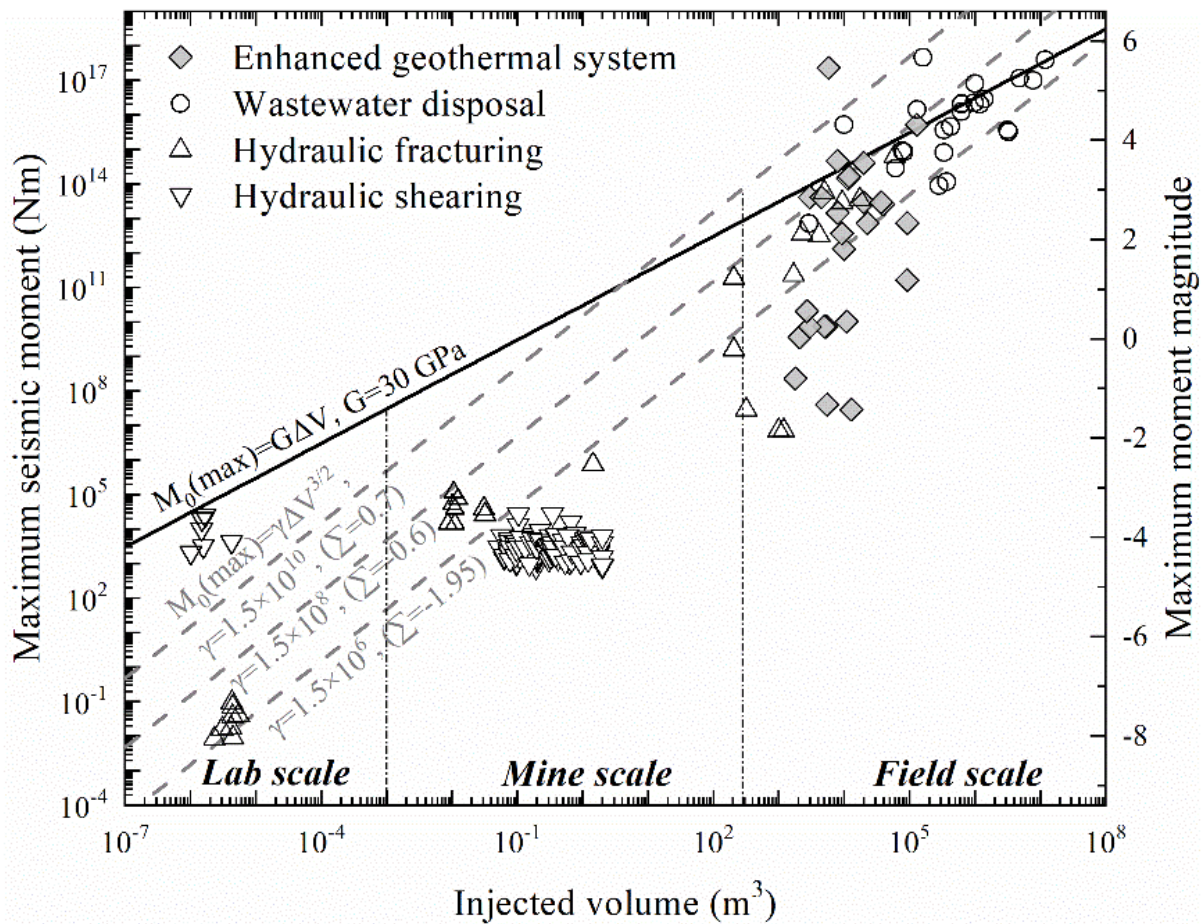
1590



1591

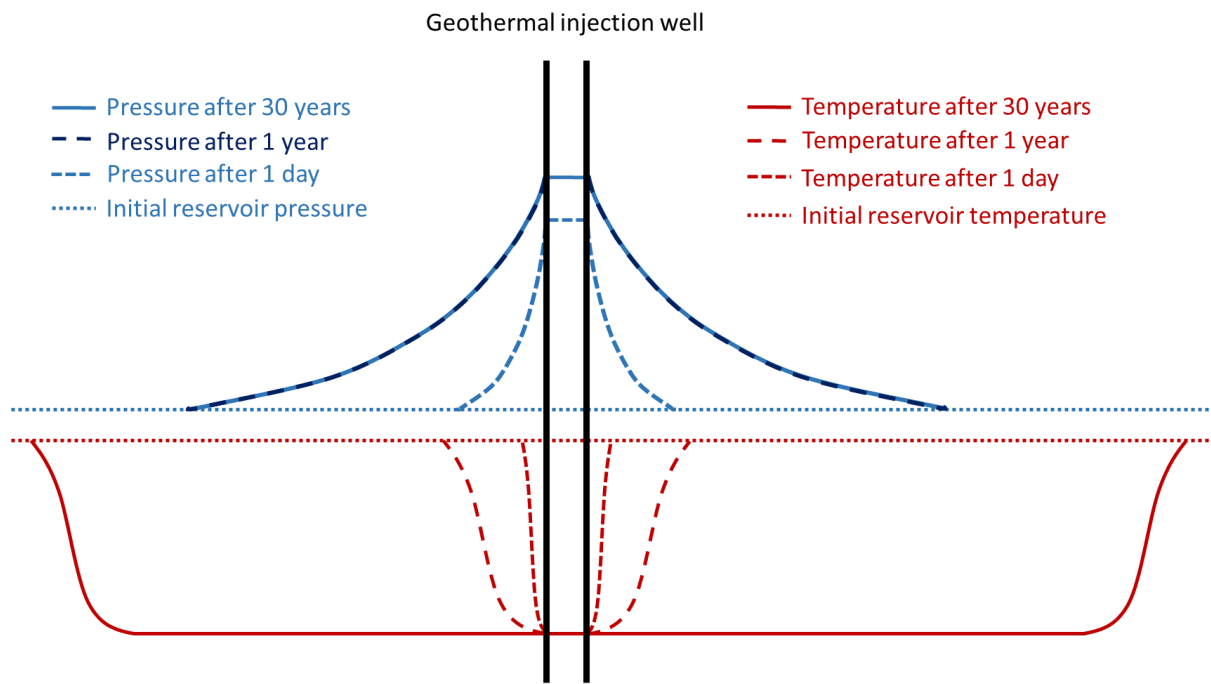
1592 *Figure 4: Ratio of thermoelastic and poroelastic stress change for Flechtinger Sandstone (rock*
 1593 *properties from Hassanzadegan et al., 2012) resulting from different temperature and pressure*
 1594 *changes.*

1595



1596

1597 *Figure 5: Maximum seismic moment as a function of injected volume in various scales. The*
 1598 *three models (four lines) relating the maximum seismic moment and injected volume are*
 1599 *proposed by McGarr (2014), van der Elst et al., (2016), and Galis et al., (2017). The lab scale*
 1600 *hydraulic shearing and hydraulic fracturing data are taken from Ji and Wu (2020) and*
 1601 *Goodfellow et al., (2015), respectively. The mine scale data is collected from Gischig et al.,*
 1602 *(2019). The field scale data of Enhanced geothermal system (EGS), wastewater disposal and*
 1603 *hydraulic fracturing are from Buijze et al., (2015), Galis et al., (2014), and McGarr (2014).*



1604

1605 *Figure 6: Schematic representation of a typical pressure and temperature profile*
 1606 *around a geothermal injection well at different times. Normally, after less than 1 year a new*
 1607 *hydraulic equilibrium is reached between injection and production well. Pressure is highest*
 1608 *close to the well and drops significantly with radial distance. Resulting effective stress changes*
 1609 *thus also drop significantly with distance from injection well. Temperature changes are*
 1610 *confined to an area relatively close to the injection well during early times. Later, while the*
 1611 *pressure does not change anymore, the cold-water front continues to move away from the well*
 1612 *with almost the same temperature everywhere inside the cold-water plume. Thus, thermoelastic*
 1613 *stress changes also have a similar magnitude everywhere in the affected volume. Additionally,*
 1614 *the temperature front may grow beyond the volume affected by relevant pressure changes.*

1615

1616 **Tables**

1617 *Table 1: Summary of hydraulic shearing tests at mine scale.*

Faulted rock type	Depth	Stress state	Injected volume (m ³)	Maximum seismic moment (Nm)	Location	Reference
Fault intersecting the Opalinus Clay	300 m	$\sigma_1=9.5$ MPa $\sigma_2=6.0$ MPa $\sigma_3=4.7$ MPa	-	-	Mont Terri Underground Research Lab (URL), Switzerland	Jeanne et al., 2017, 2018; Guglielmi et al., 2016
Fault cutting through a carbonate formation (limestone)	282 m	$\sigma_1=6.0$ MPa $\sigma_2=5.0$ MPa $\sigma_3=3.0$ MPa	2.01	7.8×10^2 - 2.7×10^4	Low Noise Underground Lab (LSBB), Laboratoire Souterrain à Bas Bruit, southeast France	Guglielmi et al., 2015a; Derode et al., 2015; Duboeuf et al., 2017; De Barros et al., 2018
Fault in shales	~180 m	$\sigma_1= 4 \pm 2$ MPa $\sigma_2= 3.8 \pm 0.4$ MPa $\sigma_3= 2.1 \pm 1$ MPa	3.20	8.1×10^2 - 3.5×10^3	Tournemire URL, Southern France	Guglielmi et al., 2015b; De Barros et al., 2016

1618

1619

1620

1621

1622

1623

1624

1625

1626

1627

1628 *Table 2: Thermo- and poroelastic properties of various rock types (α Biot's coefficient, β linear*
 1629 *thermal expansion coefficient, K bulk modulus of saturated rock).*

	β (10^{-6} 1/°C)	α	K (GPa)	References
Flechtinger sandstone	9.1	0.735	15.9	Hassanzadegan et al. (2012)
Upper Jurassic Malm limestone	6.3	0.635	23.5	Pei et al. (2020) Pei et al. (2018)
Westerly granite	7.7	0.470	25.0	Zimmerman (2000) Wong & Brace (1979)

1630